Exploring the Born-Oppenheimer surface of small and medium-sized Si clusters using the dual minima hopping method

Inauguraldissertation

zur
Erlangung der Würde eines Doktors der Philosophie
vorgelegt der
Philosophisch–Naturwissenschaftlichen Fakultät
der Universität Basel

von

Waldemar Vladimir Hellmann
aus Bonn, Deutschland

Basel, 2007

Genehmigt von der Philosophisch-Naturwissenschaftlichen Fakultät
auf Antrag von:

Prof. Dr. Stefan Goedecker

Prof. Dr. Christoph Bruder

Basel, 24. Oktober 2006 Prof. Dr. Hans-Peter Hauri (Dekan)

A mes parents

Je refuserai désormais de juger l'homme sur les formules qui justifient ses décisions. On se trompe trop aisément sur la caution des paroles, comme sur la direction des actes. Celui qui marche vers sa maison, j'ignore s'il marche vers la querelle ou vers l'amour. Je me demanderai : Quel homme est-il ? Alors seulement je connaîtrai vers où il pèse et où il ira.

Antoine de Saint Exupéry

Summary

Silicon is the most important semiconducting material in the microelectronics industry. The determination of the structure of silicon clusters is an important task since current trends of the semiconductor industry have led to a dramatic decrease of the device features. The properties of silicon clusters are peculiar and differ strongly with size. Since direct determination of the structure of clusters is not possible, Si clusters have been extensively studied using a combination of computational simulation and experimental techniques such as ion mobility measurements, polarizability measurements, Raman or IR spectroscopy. Nevertheless, agreement about the structure of the most promising global minimum candidate has been found only for silicon clusters Si_n with $n \leq 7$. Though existing global optimization methods were successful in correctly predicting the presence of structural motifs such as Si_6, Si_7 and Si_{10} subunits in low energy isomers of silicon clusters with more than 10 atoms, they were not always able to predict structures that would reproduce all the experimentally observed properties.

In this dissertation, we present a new global optimization method which we shall call the dual minima hopping method (DMHM). The method was implemented in collaboration with Stefan Goedecker. The DMHM allows us to find the global minimum of the potential energy surface (PES) within density functional theory (DFT) for systems for which a less accurate calculation of the PES is possible. The DMHM does not involve thermodynamics and can rapidly find the ground state configuration within DFT by performing a systematic search. It is based on the recently developed minima hopping method (MHM). The DMHM couples a fast approximate method such as force field or tight binding scheme with the slow but accurate DFT method. The DMHM is very efficient since it requires only an affordable number of DFT geometry optimizations for reasonable configurations which were obtained by the geometry optimization with a fast method and for which the DFT programs converge without problems.

We apply the new method to silicon clusters Si_n in the range $7 \leq n \leq 19$ by choosing a tight-binding scheme as fast approximate method and find a number of new low energy isomers within DFT for Si_{13}, Si_{16}, Si_{17}, Si_{18} and Si_{19}. We challenge the unique ground state structure for certain Si clusters Si_n with $n \geq 13$ by performing DFT calculations using the DMHM and by comparing the DFT results with the Quantum Monte Carlo (QMC) calculations done by Richard Hennig. We show on the basis of the DFT calculations which are done using the PBE exchange-correlation functional that the lowest ten

isomers coexist within a tiny energy interval. In particular, for Si_{13} the ten lowest pure isotope-free isomers coexist within less than 10 mHa. Besides, we find more than 150 different pure isotope-free low energy isomers for Si_{13}. The presence of the ^{29}Si isotope increases this number even further. We observe that the low-lying isomers for silicon clusters Si_n in the range $13 \leq n \leq 19$ can be both prolate, oblate and spherical. For some clusters the DFT and QMC energy differences are so small that entropy effects can change the energetic ordering. In particular, pure isotope-free configurations with rotational symmetry are disfavored by the entropy effects as compared to non-symmetric pure isotope-free configurations. Symmetric configurations containing one ^{29}Si isotope are disfavored by the entropy effects as compared to non-symmetric configurations containing one ^{29}Si isotope. From these observations we conclude that for silicon clusters Si_n in the range $13 \leq n \leq 19$ a mixture of several configurations with different shapes is to be expected at room temperature, and that interpretation of any experimental data should therefore be handled with great care.

Contents

Chapter 1

Introduction

The determination of the structure of Si clusters is an important task since Si clusters may find applications in the rapidly developing field of nanotechnology. Silicon is the second most abundant element after oxygen in the Earth's crust, making up 25.7% of it by mass. It has atomic number 14 and was first identified by Antoine Lavoisier in 1787. It occurs in nature mainly in minerals consisting of practically pure silicon dioxide SiO_2 in different crystalline forms. Silicon is a semiconductor with a band gap of 1.09 eV. The conductivity of silicon can be varied by doping. Crystalline silicon has melting temperature of 1687 K. Silicon valence shell has 4 electrons and the configuration $3s^2 3p^2$. The stable isotopes of silicon are ^{28}Si, ^{29}Si and ^{30}Si. The predominant isotope ^{28}Si has abundance of ∼92.2 %, the isotope ^{29}Si has abundance of ∼4.6 %, and the isotope ^{30}Si has abundance of ∼3.0 % [1]. The miniaturization trends of the semiconductor industry have decreased the device features to ∼150 nm.With Si-Si distance of around 2.4 Angstroem, the roughly estimated number of Si atoms aligned in a linear chain would be ∼600. The device features approach thus the size of silicon clusters. Silicon clusters take intermediate place between single Si atoms and small Si molecules on the one hand and bulk matter, i.e. crystalline diamond structure, on the other hand. Their properties are often peculiar and different from those of their constituent parts and from those of bulklike macroscopic pieces of matter. In particular, their properties differ dramatically with size. There is an ongoing debate about the size at which the most favorable low energy Si clusters adopt the diamond structure. Yu et al. [2] have found indications that the transition to crystalline structures occurs at around 400 atoms. Si clusters are produced with laser vaporization source from a supersaturated vapor of the material. The determination of the structure of silicon clusters is a difficult task. Standard experimental techniques such as X ray diffraction, NMR or STM are not applicable to clusters. The main source of experimental information, ion mobility measurements [3], provides only crude information about the shape of the cluster. Computational simulation is therefore necessary in order to determine the geometries of the experimentally observed clusters. From the theoretical point of view the ground state structure is determined by the global minimum of the

Born-Oppenheimer potential energy surface (PES). According to the Boltzmann distribution the global minimum structure will dominate in an ensemble of configurations if the temperature is low enough. Finding the global minimum of a high dimensional function is a difficult task and requires a systematic global optimization algorithm. Nevertheless, even best algorithms fail to guarantee that the global minimum will be found. Another problem is that calculating the Born-Oppenheimer surface with high precision is a very demanding task and usually requires some kind of approximation. Density functional theory (DFT) is one of the mostly used and computationally affordable approximations to calculate the energy of atomic clusters. A number of different global optimization algorithms has been applied to Si clusters and there was a general agreement about the lowest energy candidate structures for Si clusters consisting of up to 19 atoms. New global minimum candidates were recently proposed by Hartke [4] and Zeng [5] for silicon clusters Si_n in the range $11 \leq n \leq 19$. This shows that present global minimum algorithms are still not capable to predict the global minimum within a given exchange-correlation functional with high likelihood. Besides, different exchange-correlation functionals may change the energy order [6]. The mostly used global minimum algorithms are genetic algorithms [7], [8], [9], the basin hopping method [10], [11], simulated annealing [12], [13] and the big-bang method [14]. A.Tekin and B.Hartke [15] have calculated energies for the lowest energy structures of silicon clusters Si_n with $n \leq 29$ using DFT/B3LYP and LMP2 levels of theory with sufficiently large basis sets and have shown that the energy order of the low-lying isomers changes when employing LMP2 instead of DFT/B3LYP level of theory. They have concluded from their calculations that higher level of theory is needed in order to decide which of the proposed candidates is the true global minimum. Though new low-lying isomers have been permanently proposed, disagreement between experimentally observed and calculated polarizabilities and dissociation energies for silicon clusters Si_n with $n \leq 19$ could not be resolved. The overall agreement between theoretically calculated and experimentally observed ion mobilities is either not a proof of successful global minimum search since ion mobilities give only crude information about the shape of the cluster.

The disagreement between different researchers about the global minimum candidates for silicon clusters Si_n in the range $7 \leq n \leq 19$ was the motivation for this doctoral thesis. As we shall see later in this work, already for Si_{13} cluster at least 10 low-lying isomers lie within the DFT/PBE energy interval of 10 mHa. Searching for the global minimum of silicon clusters Si_n, most researchers have adopted an approach where one first performs a systematic search with an algorithm which allows a fast but inaccurate calculation of the potential energy surface (PES) to obtain low-lying isomers which are global minimum candidate structures. Which of the candidate structures is lowest in energy is subsequently determined in a second step by DFT calculations. Other researchers have coupled systematic search algorithms with DFT methods, but their algorithms were biased or required too many DFT calculations to be feasible within finite amount of time. In this PhD thesis we present a new method based on the minima hopping method [16] (MHM), which we will refer to as the dual minima hopping method (DMHM). The method allows to find the global minimum of the potential energy surface (PES) within density functional theory

for systems for which a fast but less precise evaluation of the PES is possible. We apply the method to silicon clusters Si_n with less than 20 atoms. Even though these systems have already been extensively studied, we find new global minimum candidates for Si_{13}, Si_{16} and Si_{19} as well as new low-lying isomers for Si_{13}, Si_{16}, Si_{17} and Si_{18}.
When investigating Si clusters, the range $13 \leq n \leq 19$ is particularly interesting because the isotopes ^{28}Si and ^{29}Si have an abundance of $\sim$92% [1] and $\sim$5% [1] respectively. On average, one of 18 Si atoms will be an isotope ^{29}Si. Pure isotope-free configurations consisting only of ^{28}Si isotopes will be present in an ensemble of configurations of silicon clusters with up to 19 atoms: most clusters in the range $13 \leq n \leq 19$ will contain no ^{29}Si isotope, one ^{29}Si isotope or two ^{29}Si isotopes. Symmetric configurations containing one ^{29}Si isotope and isotope-free configurations with rotational symmetry will be closer investigated in this thesis. Since rotational degrees of freedom are excited already at very low temperatures, and the symmetry is not destroyed due to vibrational-rotational coupling and centrifugal forces in the temperature range up to the melting point of clusters, symmetric configurations will be entropically disfavored at room temperatures as we shall show. Both isotope presence effects and rotational entropy contributions can change the energy order of silicon clusters at room temperature.
In Chapter 2 we give an overview over experimental studies of silicon clusters performed so far. These studies encompass ion mobility measurements (IMM), dissociation studies, chemical reactivity studies, ionization potential studies, photoelectron spectroscopy studies and polarizability measurements. In Chapter 3 we briefly present the fundamentals of the density functional theory (DFT). In Chapter 4 we give an overview over the basic global optimization algorithms that were used so far in the global minimum studies of silicon clusters. In chapter 5 we present the main theoretical studies of Si clusters with up to 45 atoms. The heart of this PhD thesis are Chapters 6 and 7. In Chapter 6 we present in detail the dual minima hopping method (DMHM) and its implementation for Si clusters on the basis of the tight-binding scheme developed by T.Lenosky [17]. In Chapter 7 we study the coexistence of low-lying isomers for Si_n clusters in the range $7 \leq n \leq 19$. In particular, we investigate entropy effects on the energy order. In the conclusion we summarize the results of our investigations and make suggestions for future work.

Chapter 2

Experimental studies of silicon clusters

The standard experimental techniques such as NMR for studying molecules or X ray diffraction for studying periodic systems are not applicable to clusters. Available experimental techniques give only indirect information about the structure of a cluster so that the exact positions of the atoms forming the cluster remain unknown. For this reason a combination of theoretical predictions and experimental techniques must be used in order to determine the cluster structures. Besides, the interpretation of experimental measurements must be handled with care. When comparing theoretical predictions with experiment, one should know the exact preparation conditions of the experimentally studied clusters and take into account entropy effects since as we shall see later in Chapter 7 it is not necessarily the global minimum structure of the Born-Oppenheimer potential energy surface that dominates in an ensemble of clusters at finite temperatures. Up to now, experimental studies combined with the predictions of simulations succeeded only in elucidating the geometries of small Si clusters with less than 8 atoms. For larger clusters, there is still no agreement between experimentally observed properties and those calculated for the presumable global minimum candidates obtained by simulation. According to experimental studies, Si_n clusters in the size range $20 \leq n \leq 30$ undergo a structural transition from prolate to spherical. The most important experimental techniques carried out for Si clusters encompass ion mobility measurements, dissociation studies, polarizability measurements, chemical reactivity experiments, ionization potential measurements, photoelectron spectroscopy, Knudsen mass spectrometry, calorimetric measurements, Raman and IR spectroscopy. We present in this chapter the main experimental studies of Si clusters and discuss briefly the theoretical approaches which were used to interpret the experimental results.

2.1 Ion Mobility Measurements

Ion mobility measurements (IMM), which can be performed only for charged clusters, are considered today as one of the best techniques to provide information about the cluster structure [18]. The mobility of a gas phase ion determines how rapidly it moves through a buffer gas under the influence of an electric field. The mobility of an ion depends on its average collision cross section with the buffer gas and thus on the geometry of the ion. A spherical structure will have a larger mobility than a non-spherical structure thus allowing to separate spherical from non-spherical isomers. The structural information obtained from IMM provides only information about the outer shape of the ion, but not about its inner structure, since inner atoms are shielded by the outer atoms and therefore do not participate in collisions with the buffer gas. Structural assignments for unknown species studied in the ion mobility experiments become possible by comparison of the measured mobilities with mobilities calculated for candidate geometries. The high-resolution configuration [19] for performing ion mobility experiments consists of four main regions: (1) the source, where the clusters are produced; (2) the ion gate, which connects the source to the drift tube and prevents neutral species from entering the drift tube; (3) the drift tube and (4) the mass spectrometer and the ion detector. The source is a laser vaporization source with a near static buffer gas. The buffer gas in the source is around 500 Torr. Clusters are produced by laser vaporization of a target of the material to be studied. Subsequently, cluster ions are guided from the target rod towards the entrance of the ion gate by a shaped electric field. By varying the voltage on the rod, one can adjust the residence time of clusters in the source and vary the cluster size distribution. By reversing the voltages it is possible to extract either anions or cations. The function of the ion gate is to allow ions to pass from the source into the drift tube while preventing neutral species from entering the drift tube. This is accomplished by a uniform electric field to carry the ions through the ion gate and a counterflow of buffer gas to prevent neutral species from passing through. A uniform electric field is generated along the axis of the drift tube. At the end of the drift tube the ions are carried by the buffer gas through a small hole into the vacuum chamber. Using this arrangement one can perform measurements in the temperature range from -25 to +100 ℃. After exiting the drift tube, the ions are accelerated and focused by a set of electrostatic lenses. The ions are directed through a 0.5-cm-diam. aperture into a chamber that houses a quadrupole mass spectrometer and an ion detector. At the end of the quadrupole, ions are detected by an off-axis collision dynode and dual microchannel plates. Drift time distributions are recorded by measuring the arrival time distribution at the detector, with a start pulse provided by the vaporization laser. Ion mobility measurements were successfully applied to study the structure of Si_n clusters [20], [21], [19], [3], [22] and have provided strong evidence for prolate to spherical transition in the size range $20 \leq n \leq 30$ [20]. The high-resolution ion mobility experiments [19] performed by Hudgins et al. [3] have shown that starting with Si_{17}^+ several low-lying isomers can be resolved at room temperature.

2.2 Dissociation studies

Jarrold and Bower [23] have performed collision-induced dissociation studies of silicon cluster ions with argon. The collision energy was chosen low enough in order to prevent excited electronic states and to favor the dissociation on the ground-state potential energy surface via the lowest energy dissociation channel. They have observed that for clusters with $n < 15$ the dominant products are Si_6^+ and Si_7^+, whereas for larger clusters the dissociation took place by loss of the Si_{10}^+ ion. The results obtained in these studies were similar to those obtained in the photodissociation studies by Smalley [24]. Photodissociation involves excitation to an excited electronic state, so that the observed similarity in product distribution with collision-induced dissociation indicates that the excitation is followed during the dissociation by the relaxation to the electronic ground state. Jarrold and Honea [25] have studied multi-collision dissociations of silicon cluster ions containing up to 70 atoms. The ions in the drift tube undergo many collisions with the collision gas, and each collision converts a fraction of the kinetic energy of the ion into internal energy. Because of the averaging that occurs in the multicollision excitation process the resulting energy distribution is narrow. Si_n clusters with $19 \leq n \leq 35$ have been observed dissociating mainly by loss of Si_{10} species, larger clusters dissociated by Si_6-unit loss. Dissociation energies have been estimated from the experimental results. Shvartsburg, Jarrold et al. [26] have modeled the dissociation of Si_n neutrals and cations in the range $2 \leq n \leq 26$. They have calculated dissociation energies for different fragmentation pathways using the gradient-corrected Perdew-Wang-Becke 88 (PWB) functional and have compared the dissociation energies of lowest energy pathways with the experimental values [25]. The computed dissociation energies were in good agreement with experiment, though discrepancies for Si_{13} and Si_{19} were observed.

2.3 Polarizability studies

The static polarizabilities of Si_n clusters with $9 \leq n \leq 120$ have been experimentally investigated in dependence on cluster size by R.Schäfer et al. [27]. They have observed that the polarizability per atom as a function of cluster size varies irregularly around the bulk limit of 3.71 $\mathring{A}^3$. The largest polarizability was observed for Si_{10}. The clusters are produced by a pulsed laser vaporization cluster source. The clusters leave the source through a nozzle and form a molecular beam. The deflections are measured for each cluster size using a collimated ionization laser beam which scans the cluster beam. We obtain thus size selective cluster beam profiles by detecting the ionized clusters with a mass spectrometer for each scanning position.
Several researchers [28, 29, 30, 31] have calculated the polarizabilities within density functional theory of the most promising global minimum candidates of silicon clusters. Jackson et al. [28] have calculated static polarizabilities of Si_n clusters with $n = 10, 13, 20, 21$ using the LDA approximation. As compared to the experimental results of R.Schäfer, only

a partial agreement was observed. Vasiliev et al. [29] have calculated polarizabilities of small Si_n clusters with $3 \leq n \leq 10$ using higher-order finite-difference pseudopotential plane-wave technique. They have observed that the computed polarizabilities per atom tend to decrease with increasing cluster size and approach the bulk limit from above. In order to compare their results with the experimental data, they have taken into account an additional contribution from the dipole rotating in external electric field. Nevertheless, they couldn't reproduce the experimental polarizabilities of R.Schäfer. Bazterra et al. [30] have calculated polarizabilities of Si_n clusters with $3 \leq n \leq 13$ using the hybrid functional B3PW91 [32], [33]. Except for Si_{10}, their polarizabilities for Si_9-Si_{13} were larger than those of R.Schäfer. Since they have got similar values for the polarizabilities as Jackson et al., they have concluded from the discrepancies that the experimental values are likely to be incorrect. Recently, C.Pouchan et al. [31] have performed polarizability calculations for Si_3-Si_{10} clusters using the LDA/VWN (local density approximation/Vosko-Wilk-Nusair), BLYP and B3LYP exchange correlation functionals. Their polarizabilities are similar to those obtained by I.Vasiliev and V.Bazterra. C.Pouchan et al. have also studied the relationship between the polarizability and the HOMO-LUMO gap. According to simple perturbation theory using the one-electron wave functions, the value of polarizability can be calculated according to

$$\alpha_{ii} = 2 \sum_{l,k} |\langle k|\mu_i|l\rangle|^2 / (E_l - E_k) \qquad , \tag{2.1}$$

where l and k stand for the unoccupied (or antibonding) and the occupied (or bonding) orbitals, respectively. The matrix element corresponds to the size of the transition dipole moment. In the first approximation one can say that larger polarizabilities correlate with smaller HOMO-LUMO gaps since it contributes most significantly to α_{ii} in the equation 2.1. C.Pouchan et al. have found in their studies that the polarizability of silicon clusters is not directly related to the size of the HOMO-LUMO gap, but to the size of the energy gap between symmetry-compatible bonding and antibonding molecular orbitals. To summarize, neither of the theoretical calculations of polarizabilities [28], [29], [30], [31] did succeed in reproducing the experimental data of R. Schäfer. These discrepancies indicate that either the experimentally studied structures or the theoretically studied isomers of silicon clusters are not the true global minima of the Born-Oppenheimer potential energy surface.

2.4 Chemical reactivity studies

J.L.Elkind et al. [34] have studied chemical reactivity of silicon clusters towards ammonia (NH_3) and have found that silicon clusters with 21, 25, 33, 39 and 45 atoms appeared to be inert. L.Anderson, S.Maruyama and R.Smalley [35], [36] have studied chemical reactivity

of silicon cluster ions towards ethylene (C_2H_4) and have found that silicon cluster ions with 39 and 45 atoms are particularly unreactive. From these studies it appeared that chemical reactivity has strong variations as a function of cluster size. Recently, R.L.Zhou and B.C.Pan have performed simulations [37] combining a tight-binding approach and LDA calculations, and have proposed a global minimum candidate structure for the Si_{45} cluster which is also a candidate for the lowest reactivity candidate structure. They have argued that isomers showing low reactivity are those with a small number of dangling bonds in the outer cage of the isomer. Such isomers are those with a small number of threefold-coordinated Si atoms which have one dangling bond and are very active and a large number of fivefold-coordinated Si atoms and fourfold-coordinated Si atoms. However, this theoretical work does not explain why low chemical reactivity was observed experimentally for silicon clusters with 39 and 45 atoms. The results of M.Jarrold et al. [38], [39] differ from those of Smalley. M.Jarrold et al. have studied the chemical reactivity of Si_n^+ clusters in the range $3 \leq n \leq 50$ towards ethylen and have found that there appears nothing to be unique about Si_{39}^+ and Si_{45}^+. The studies [39] which they have performed for the Si_n^+ clusters in the range $11 \leq n \leq 50$ suggested the presence of structural isomers for virtually all clusters. The presence of isomers became apparent from studies of reaction kinetics since structural isomers react at significantly different rates. The measurements of chemical reactivity towards ethylene have indicated that the reactions with C_2H_4 are more sensitive to the cluster structure than the reactions with NH_3 and involve specific localized sites on the cluster. M.Jarrold et al. have also studied chemical reactivity towards oxygen [40] and towards water [41] of Si_n^+ clusters ions with $10 \leq n \leq 65$. They have observed large variations in the reactivity of the smaller clusters and have found that Si_{13}^+, Si_{14}^+ and Si_{19}^+ are particularly inert. The variations in reactivity are rapidly damped with increasing cluster size and for clusters with $40 \leq n \leq 65$ the reactivity is nearly independent of size.

2.5 Ionization potential studies

Experimental ionization potential (IP) measurements [42], [43] based on the photoionization method have been performed for Si_n clusters in the range $2 \leq n \leq 200$. One can possibly distinguish the theoretically predicted low-lying isomers by comparing the calculated ionization potentials for these isomers with the experimentally observed values. Trevor et al. [42] have concluded from the photoionization mass spectrum (PMS) of silicon clusters that the IPs of Si_{2-7} and Si_{10} are found to be grater than 7.87 eV while Si_{22}-Si_{100} have IPs between 4.99 and 6.42 eV. Besides, Si_{6-11}^+ are found to be dominant photofragments from the larger silicon clusters. K.Fuke et al. [43] have measured the IPs of Si_n clusters in the interval $4 \leq n \leq 200$ and have identified major maxima at $n = 10$ and 20. They have observed a large gap in IPs between $n = 20$ and 22 and have ascribed it to the structural transition in this size range. Jarrold et al. [44] have performed a systematic ground state geometry search and have calculated the IPs for the best global minimum

candidates. The calculated IPs reproduced the experimentally observed size-dependent trends.

2.6 Photoelectron spectroscopy

Photoelectron spectroscopy is a powerful tool for studies of atomic clusters since it probes both the geometry and the electronic structure. In photoelectron spectroscopy the anion is photoexcited above the detachment threshold and the energy of the released electrons is measured. The two characteristic values which one obtains from the photoelectron spectrum are the threshold value which indicates the adiabatic electron affinity (AEA) and the maximum of detachment efficiency energy which is the vertical detachment energy (VDE). The vertical detachment energy is the energy needed to remove an electron from the HOMO. In metal clusters the HOMO-LUMO gap decreases with increasing cluster size rendering the clusters metallic. Müller et al. [45] have measured the photoelectron spectra (PES) for silicon cluster anions Si_n^- with $n \leq 20$. Besides, they have modeled the PES for a number of low-energy isomers using density functional theory. The simulated PES gave an excellent agreement with the experiment. Müller et al. have calculated the HOMO-LUMO gap for Si_n neutrals and have found that the band gap does not decrease with increasing n as it would be the case for metallic species. O.Cheshnovsky et al. [46] performed ultraviolett photoelectron spectroscopy (UPS) measurements on the negatively charged silicon clusters Si_n^- with $n \leq 12$. N.Binggeli et al. [47] have calculated PES spectra of small Si_n^- with $n \leq 7$ and have found a good agreement between theoretical results and the experimental data [46]. By comparing the theoretical and the experimental spectra, they were able to distinguish between the two low-energy isomers of Si_6. Recently, G.Meloni et al. [48] have obtained PES for silicon cluster anions Si_n^- with $4 \leq n \leq 34$. Their data has shown trends which are consistent with the structural transformation from prolate to spherical in the range $20 \leq n \leq 30$, though they have observed a signal from the prolate structure even for Si_{35}^-.

2.7 Other experimental studies

R.Schmude and Q.Ran [49], [50] have investigated the thermodynamic properties of Si_2, Si_3 and Si_5 molecules using Knudsen mass spectrometry which is a technique for studying the equilibrium between condensed and vapor phases. From their measurements they have calculated the atomization and formation enthalpies of the investigated clusters. T.Bachels et al. [51] have calorimetrically determined the binding energies per atom of neutral silicon clusters in the range $N = 65$ to $N = 890$. The measurements of the binding energies were performed within a molecular beam experiment, in which the released heat during the deposition of Si clusters on a Si surface was measured with a pyroelectric thin

film calorimeter. The measured binding energies indicated the existence of two different classes of cluster isomers: one with spherical-like geometries characterized by binding energies proportional to $N^{-1/3}$, and the other showing no dependence on the cluster size in the investigated size range. Thus, the prolate to spherical transition already observed in ion mobility measurements [20] was confirmed by the measurements of the binding energies. E.Honea et al. [52] have obtained Raman spectra of Si_4, Si_6 and Si_7 clusters and have concluded from these spectra that Si_4 is a planar rhombus, Si_6 a distorted octahedron and Si_7 a pentagonal bipyramid. S.Li et al. [53] have obtained the IR spectra of silicon clusters. K.Jackson et al. [54] have calculated Raman- and IR-active frequencies and intensities for several silicon clusters using the local density approximation (LDA). For the smaller clusters Si_n with $3 \leq n \leq 8$ their results were in good agreement with experimental measurements.

Chapter 3

The fundamentals of density functional theory

Density functional theory (DFT) is presently the most successful and the most widely used approach to compute the electronic structure of matter. Whereas for small systems methods of contemporary quantum chemistry such as restricted and unrestricted Hartree-Fock models, configuration interaction and many-body perturbation methods provide predictions of properties of both excited and ground states of molecules with a high accuracy, these methods become computationally too expensive for large systems. Density functional theory provides in its original formulation an effective approach based on the knowledge of the electron density to calculate the ground state properties of a system. The applicability of DFT ranges from atoms and molecules to solids. DFT predicts correctly a great variety of properties such as molecular geometries, ionization energies, vibrational frequencies and polarizabilities. In the course of time the original DFT has been generalized to deal with more complex problems such as spin polarized systems, relativistic electrons or time-dependent phenomena.

3.1 The molecular many-electron Schrödinger equation

The basic task of solid state physics and quantum chemistry is the solution of the time-independent non-relativistic Schrödinger equation

$$\hat{H}\Psi_i(\vec{x}_1, \vec{x}_2, ..., \vec{x}_N, \vec{R}_1, \vec{R}_2, ..., \vec{R}_M) = E_i\Psi_i(\vec{x}_1, \vec{x}_2, ..., \vec{x}_N, \vec{R}_1, \vec{R}_2, ..., \vec{R}_M). \tag{3.1}$$

$\hat{H}$ denotes the Hamilton operator in atomic units for a system consisting of M nuclei and N electrons:

$$\hat{H} = -\frac{1}{2}\sum_{i=1}^{N}\nabla_i^2 - \frac{1}{2}\sum_{A=1}^{M}\frac{1}{M_A}\nabla_A^2 - \sum_{i=1}^{N}\sum_{A=1}^{M}\frac{Z_A}{r_{iA}} + \sum_{i=1}^{N}\sum_{j>i}^{N}\frac{1}{r_{ij}} + \sum_{A=1}^{M}\sum_{B>A}^{M}\frac{Z_A Z_B}{R_{AB}}. \tag{3.2}$$

Here, the indices A and B run over the M nuclei, while i and j run over the N electrons. The first two terms describe the kinetic energy of the electrons and nuclei. The other three terms represent the attractive electrostatic interaction between the nuclei and the electrons and repulsive potential due to the electron-electron and nucleus-nucleus interactions. The Born-Oppenheimer approximation states that due to their masses the nuclei move much slower than the electrons and that therefore we can consider the electrons as moving in the filed of fixed nuclei. The nuclear kinetic energy can be neglected and the potential energy of the nuclei is a constant. The electronic Hamiltonian is given by

$$\hat{H}_{elec} = -\frac{1}{2}\sum_{i=1}^{N}\nabla_i^2 - \sum_{i=1}^{N}\sum_{A=1}^{M}\frac{Z_A}{r_{iA}} + \sum_{i=1}^{N}\sum_{j>i}^{N}\frac{1}{r_{ij}} = \hat{T} + \hat{V}_{Ne} + \hat{V}_{ee} \tag{3.3}$$

and the corresponding electronic Schrödinger equation for fixed R_{AB} is given by

$$\hat{H}_{elec}\Psi_{elec} = E_{elec}\Psi_{elec}. \tag{3.4}$$

The total energy E_{tot} is then the sum of E_{elec} and the constant nuclear repulsion term E_{nucl}:

$$E_{tot} = E_{elec} + E_{nucl} \text{ with } E_{nucl} = \sum_{A=1}^{M}\sum_{B>A}^{M}\frac{Z_A Z_B}{R_{AB}}. \tag{3.5}$$

3.2 The variational principle for the ground state

When a system is in the state Ψ, the expectation value of the energy is given by

$$E[\Psi] = \frac{<\Psi|\hat{H}|\Psi>}{<\Psi|\Psi>} \text{ with } <\Psi|\hat{H}|\Psi> = \int \Psi^*\hat{H}\Psi d\vec{x}. \tag{3.6}$$

The variational principle states that the energy computed from a guessed Ψ is an upper bound to the true ground-state energy E_0. Full minimization of the functional E[Ψ] with respect to all allowed N-electrons wave functions will give the true ground state Ψ_0 and energy $E[\Psi_0] = E_0$, that is

$$E_0 = \min_\Psi E[\Psi] = \min_\Psi < \Psi|\hat{T} + \hat{V}_{Ne} + \hat{V}_{ee}|\Psi > . \tag{3.7}$$

For a system of N electrons and given nuclear potential V_{ext} (which replaces the potential V_{Ne}), the variational principle defines a procedure to determine the ground-state wave-function Ψ_0, the ground-state energy $E_0[N, V_{ext}]$, and other properties of interest. In other words, the ground state energy is a functional of the number of electrons N and the nuclear potential V_{ext}:

$$E_0 = E[N, V_{ext}]. \tag{3.8}$$

3.3 The Hartree-Fock approximation

Suppose that the ground state function Ψ_0 is approximated as an antisymmetrized product of N orthonormal spin orbitals $\psi_i(\vec{x})$, each a product of a spatial orbital $\phi_k(\vec{r})$ and a spin function $\sigma(s) = \alpha(s)$ or $\beta(s)$, the Slater determinant

$$\Psi_0 \approx \Psi_{HF} = \frac{1}{\sqrt{N!}} \begin{vmatrix} \psi_1(\vec{x}_1) & \psi_2(\vec{x}_1) & \cdots & \psi_N(\vec{x}_1) \\ \psi_1(\vec{x}_2) & \psi_2(\vec{x}_2) & \cdots & \psi_N(\vec{x}_2) \\ \vdots & \vdots & & \vdots \\ \psi_1(\vec{x}_N) & \psi_2(\vec{x}_N) & \cdots & \psi_N(\vec{x}_N) \end{vmatrix} . \tag{3.9}$$

The Hartree-Fock approximation is the method whereby the orthogonal orbitals ψ_i are found that minimize the energy for this determinant form of Ψ_0:

$$E_{HF} = \min_{\Psi_{HF}} E[\Psi_{HF}]. \tag{3.10}$$

The expectation value of the Hamiltonian operator with Ψ_{HF} is given by

$$E_{HF} =< \Psi_{HF}|\hat{H}|\Psi_{HF} >= \sum_{i=1}^{N} H_i + \frac{1}{2}\sum_{i,j=1}^{N}(J_{ij} - K_{ij}). \tag{3.11}$$

Here

$$H_i \equiv \int \psi_i^*(\vec{x})[-\frac{1}{2}\nabla^2 - V_{ext}(\vec{x})]\psi_i(\vec{x})d\vec{x} \tag{3.12}$$

defines the contribution due to the kinetic energy and the electron-nucleus attraction, whereas

$$J_{ij} = \int\int \psi_i(\vec{x}_1)\psi_i^*(\vec{x}_1)\frac{1}{r_{12}}\psi_j(\vec{x}_2)\psi_j^*(\vec{x}_2)d\vec{x}_1 d\vec{x}_2 \tag{3.13}$$

are called Coulomb integrals, and

$$K_{ij} = \int\int \psi_i^*(\vec{x}_1)\psi_j(\vec{x}_1)\frac{1}{r_{12}}\psi_i(\vec{x}_2)\psi_j^*(\vec{x}_2)d\vec{x}_1 d\vec{x}_2 \tag{3.14}$$

are called exchange integrals. The integrals are real, and $J_{ij} \geq K_{ij} \geq 0$. We have the property $J_{ii} = K_{ii}$. The variational freedom in the expression of the energy is in the choice of the orbitals. The minimization of the energy functional with the normalization conditions $\int \psi_i^*(\vec{x})\psi_j(\vec{x})d\vec{x} = \delta_{ij}$ leads to the Hartree-Fock differential equations

$$\hat{f}\psi_i = \epsilon_i\psi_i, i = 1, 2, ..., N. \tag{3.15}$$

These N equations are eigenvalue equations, where the Lagrangian multipliers ϵ_i are the eigenvalues of the operator $\hat{f}$. The Fock operator $\hat{f}$ is an effective one-electron operator defined as

$$\hat{f} = -\frac{1}{2}\nabla_i^2 - \sum_{A=1}^{M}\frac{Z_A}{r_{iA}} + V_{HF}(i). \tag{3.16}$$

The first two terms are the kinetic energy and the potential energy due to the electron-nucleus attraction. $V_{HF}(i)$ is the Hartree-Fock potential, the average repulsive potential experienced by the i-th electron due to the remaining $N-1$ electrons, and it is given by

$$V_{HF}(\vec{x}_1) = \sum_{j}^{N}\left(\hat{J}_j(\vec{x}_1) - \hat{K}_j(\vec{x}_1)\right). \tag{3.17}$$

In this equation

$$\hat{J}_j(\vec{x}_1) = \int |\psi_j(\vec{x}_2)|^2\frac{1}{r_{12}}d\vec{x}_2 \tag{3.18}$$

is the Coulomb operator which represents the potential that an electron at position $\vec{x}_1$ experiences due to the average charge distribution of another electron in spin orbital ψ_j.

The second term is the exchange contribution to the HF potential. It has no classical analog and is defined through its effect when operating on a spin orbital:

$$\hat{K}_j(\vec{x}_1)\psi_i(\vec{x}_1) = \int \psi_j^*(\vec{x}_2)\frac{1}{r_{12}}\psi_i(\vec{x}_2)\psi_j^*(\vec{x}_1)d\vec{x}_2. \tag{3.19}$$

The HF potential is non-local and it depends on the spin orbitals. Thus, the HF equations must be solved self-consistently. Koopman's theorem provides a physical interpretation of the orbital energies: it states that the orbital energy ϵ_i is an approximation of minus the ionization energy associated with the removal of an electron from the orbital ψ_i, i.e. $\epsilon_i \approx E_N - E_{N-1}^i = -IE(i)$.

3.4 The electron density

The electron density is the central quantity in DFT. It is defined as the integral over the spin coordinates of all electrons and over all but one of the spatial variables ($\vec{x} \equiv \vec{r}, s$):

$$\rho(\vec{r}_1) = N \int \cdots \int |\Psi(\vec{x}_1, \vec{x}_2, \cdots, \vec{x}_N)|^2 ds_1 d\vec{x}_2 \cdots d\vec{x}_N. \tag{3.20}$$

$\rho(\vec{r})d\vec{r}$ determines the probability of finding any of the N electrons within volume element $d\vec{r}$. $\rho(\vec{r})$ is a non-negative function of only 3 spatial variables which vanishes at infinity and integrates to the total number of electrons:

$$\rho(\vec{r} \to \infty) = 0 \quad , \quad \int \rho(\vec{r})d\vec{r} = N \tag{3.21}$$

$\rho(\vec{r})$ is an observable and can be measured experimentally, e.g. by X-ray diffraction. At any position of an atom, the gradient of $\rho(\vec{r})$ has a discontinuity and there is a cusp:

$$\lim_{r_{iA}\to 0} \left[\nabla_r + 2Z_A\right] \bar{\rho}(\vec{r}) = 0, \tag{3.22}$$

where Z is the nuclear charge and $\bar{\rho}(\vec{r})$ is the spherical average of $\rho(\vec{r})$. The electron density $\rho(\vec{r})$ decays exponentially for large distances from all nuclei:

$$\rho(\vec{r}) \approx \exp\left[-2\sqrt{2I}|\vec{r}|\right], \tag{3.23}$$

where I is the exact ionization energy.

3.5 The first Hohenberg-Kohn theorem

1.Hohenberg-Kohn theorem: The external potential $V_{ext}(\vec{r})$ is (to within a constant) a unique functional of $\rho(\vec{r})$; since, in turn $V_{ext}(\vec{r})$ fixes $\hat{H}$, the full many particle ground state is a unique functional of $\rho(\vec{r})$.

Interpretation: The first Hohenberg-Kohn theorem demonstrates that the electron density uniquely determines the Hamiltonian operator and thus all the properties of the system.

Proof: Let us assume that there were two external potentials $V_{ext}(\vec{r})$ and $V'_{ext}(\vec{r})$ differing by more than a constant, each giving the same $\rho(\vec{r})$ for its ground state, we would have two Hamiltonians $\hat{H}$ and $\hat{H}'$ whose ground-state densities were the same although the normalized wave functions Ψ and Ψ' would be different. Taking Ψ' as a trial wave function for the $\hat{H}$ problem, we get

$$E_0 < \left\langle \Psi' | \hat{H} | \Psi' \right\rangle = \left\langle \Psi' | \hat{H}' | \Psi' \right\rangle + \left\langle \Psi' | \hat{H} - \hat{H}' | \Psi' \right\rangle = E'_0 + \int \rho(\vec{r}) \left[V_{ext}(\vec{r}) - V'_{ext}(\vec{r}) \right] d\vec{r}, \tag{3.24}$$

where E_0 and E'_0 are the ground-state energies for $\hat{H}$ and $\hat{H}'$, respectively. Similarly, taking Ψ as a trial function for the $\hat{H}'$ problem, we get

$$E'_0 \left\langle \Psi | \hat{H}' | \Psi \right\rangle = \left\langle \Psi | \hat{H} | \Psi \right\rangle + \left\langle \Psi | \hat{H}' - \hat{H} | \Psi \right\rangle = E_0 + \int \rho(\vec{r}) \left[V'_{ext}(\vec{r}) - V_{ext}(\vec{r}) \right] d\vec{r}. \tag{3.25}$$

Adding the two equations, we would obtain $E'_0 + E_0 < E_0 + E'_0$, which is a contradiction, and so two different external potentials $V_{ext}(\vec{r})$ cannot give the same $\rho(\vec{r})$ for their ground state. So, $\rho(\vec{r})$ determines N and $V_{ext}(\vec{r})$ and hence all the properties of the ground state, for example the kinetic energy $T[\rho]$, the potential energy $V[\rho]$, and the total energy $E[\rho]$. Now, we can write the total energy as

$$E[\rho] = E_{Ne}[\rho] + T[\rho] + E_{ee}[\rho] = \int \rho(\vec{r}) V_{Ne}(\vec{r}) d\vec{r} + F_{HK}[\rho] \tag{3.26}$$

with

$$F_{HK}[\rho] = T[\rho] + E_{ee}. \tag{3.27}$$

The explicit form of the functional F_{HK} is the major challenge of density functional theory. If it were known the Schrödinger equation could be solved exactly. $F_{HK}[\rho]$ contains the

functional for the kinetic energy $T[\rho]$ and that for the electron-electron interaction, $E_{ee}[\rho]$. The explicit form of both these functionals is unknown. However, from the latter we can extract at least the classical part $J[\rho]$,

$$E_{ee}[\rho] = \frac{1}{2}\int\int \frac{\rho(\vec{r}_1)\rho(\vec{r}_2)}{r_{12}} d\vec{r}_1 d\vec{r}_2 + E_{noncl} = J[\rho] + E_{noncl}[\rho]. \tag{3.28}$$

E_{noncl} is the non-classical contribution to the electron-electron interaction consisting of self-interaction correction, exchange and Coulomb correlation terms. It is the major task of the DFT to find the correct form of the functionals $T[\rho]$ and $E_{noncl}[\rho]$.

3.6 The second Hohenberg-Kohn theorem

2.Hohenberg-Kohn theorem:

$F_{HK}[\rho]$, the functional that delivers the ground state energy of the system, delivers the lowest energy if and only if the input density is the true ground state density.

Interpretation:

This is nothing but a reformulation of the variational principle:

$$E_0 = E[\rho] \leq E[\tilde{\rho}] = T[\tilde{\rho}] + E_{Ne}[\tilde{\rho}] + E_{ee}[\tilde{\rho}]. \tag{3.29}$$

Proof: The proof of this equation makes use of the variational principle established for wave functions. We recall that with the 1.Hohenberg-Kohn theorem any trial density $\tilde{\rho}$ defines its own Hamiltonian $\tilde{\hat{H}}$ and hence its own wave function $\tilde{\Psi}$. This wave function can now be taken as the trial wave function for the Hamiltonian generated from the true external potential V_{ext}. Thus,

$$\left\langle \tilde{\Psi}|\hat{H}|\tilde{\Psi}\right\rangle = T[\tilde{\rho}] + E_{ee}[\tilde{\rho}] + \int \tilde{\rho}(\vec{r})V_{ext}d\vec{r} = E[\tilde{\rho}] \geq E_0 = E[\rho] = \left\langle \Psi_0|\hat{H}|\Psi_0\right\rangle. \tag{3.30}$$

3.7 The Kohn-Sham equations

We have seen that the ground state energy of a system can be written as

$$E_0 = \min_\rho \left(F[\rho] + \int \rho(\vec{r})V_{Ne}d\vec{r} \right) \tag{3.31}$$

where the universal functional $F[\rho]$ contains the contributions of the kinetic energy, the classical Coulomb interaction and the non-classical portion:

$$F[\rho] = T[\rho] + J[\rho] + E_{noncl}[\rho] \tag{3.32}$$

Only $J[\rho]$ is known. The main problem is to find the expressions for $T[\rho]$ and $E_{noncl}[\rho]$. Kohn and Sham suggested to calculate the exact kinetic energy of a non-interacting reference system with the same density as the real, interacting one

$$T_S = -\frac{1}{2}\sum_i^N \left\langle \psi_i | \nabla^2 | \psi_i \right\rangle \ , \rho_S(\vec{r}) = \sum_i^N \sum_s |\psi_i(\vec{r}, s)|^2 = \rho(\vec{r}), \tag{3.33}$$

where the ψ_i are the orbitals of the non-interacting system. Of course, T_S is not equal to the true kinetic energy of the system. Kohn and Sham accounted for that by introducing the separation of the functional $F[\rho]$ according to

$$F[\rho] = T_S[\rho] + J[\rho] + E_{XC}[\rho], \tag{3.34}$$

where the E_{XC} given by

$$E_{XC} \equiv (T[\rho] - T_S[\rho]) + (E_{ee}[\rho] - J[\rho]). \tag{3.35}$$

is the so-called exchange-correlation energy. The exchange and correlation energy is the functional that contains everything that is unknown. The question which arises now is how can we define a potential V_S such that is provides us with a Slater determinant which is characterized by the same density as our real system. We rewrite now the expression for the energy of the interacting system as

$$E[\rho] = T_S[\rho] + J[\rho] + E_{XC}[\rho] + E_{Ne}[\rho] \tag{3.36}$$

or

$$E[\rho] = T_S[\rho] + \frac{1}{2}\int\int \frac{\rho(\vec{r}_1)\rho(\vec{r}_2)}{r_{12}} d\vec{r}_1 d\vec{r}_2 + E_{XC}[\rho] + \int V_{Ne}\rho(\vec{r}) d\vec{r} \tag{3.37}$$

The only term which is unknown is E_{XC}. The equations which minimize this energy expression under the constraint $< \psi_i | \psi_j >= \delta_{ij}$ are called the Kohn-Sham equations:

$$\left(-\frac{1}{2}\nabla^2 + \left[\int \frac{\rho(\vec{r}_2)}{r_{12}} d\vec{r}_2 + V_{XC}(\vec{r}_1) - \sum_A^M \frac{Z_A}{r_{1A}}\right]\right)\psi_i = \left(-\frac{1}{2}\nabla^2 + V_S(\vec{r}_1)\right)\psi_i = \epsilon_i\psi_i \quad (3.38)$$

with

$$V_S(\vec{r}_1) = \int \frac{\rho(\vec{r}_2)}{r_{12}} d\vec{r}_2 + V_{XC}(\vec{r}_1) - \sum_A^M \frac{Z_A}{r_{1A}}. \quad (3.39)$$

The exchange-correlation potential V_{XC} is defined as the derivative of E_{XC} with respect to ρ:

$$V_{XC} = \delta E_{XC}/\delta\rho. \quad (3.40)$$

3.8 The exchange-correlation functionals

The local density approximation (LDA) is the simplest exchange-correlation functional approximation. At the center of the model is the idea of an uniform electron gas. The electrons move in a positive background charge distribution so that the total charge is zero and the system is neutral. Within the LDA assumption E_{XC} can be written as

$$E_{XC}^{LDA}[\rho] = \int \rho(\vec{r})\epsilon_{XC}(\rho(\vec{r}))d\vec{r}. \quad (3.41)$$

$\epsilon_{XC}(\rho(\vec{r}))$ is the exchange-correlation energy per particle of an uniform electron gas of density $\rho(\vec{r})$. In the expression above the exchange-correlation energy per particle is weighted with the probability $\rho(\vec{r})$ to find an electron at this position. One can show that ϵ_{XC} can be written as the sum of exchange and correlation parts:

$$\epsilon_{XC}(\rho) = \epsilon_X(\rho) + \epsilon_C(\rho) \quad , \quad (3.42)$$

where

$$\epsilon_X(\rho) = -\frac{3}{4}\left(\frac{3\rho(\vec{r})}{\pi}\right)^{\frac{1}{3}}. \quad (3.43)$$

An expression for the correlation part $\epsilon_C(\rho)$ has been proposed by Vosko, Wilk, and Nusair(VWN) [55].

For open-shell molecules the local spin density approximation (LSDA) gives better results than LDA. Whereas in the LDA, electrons with opposite spins paired with each other have the same spatial Kohn-Sham orbital, LSDA allows such electrons to have different spatial Kohn-Sham orbitals. The generalization of density-functional theory that allows different orbitals for electrons with different spins is called spin-density functional theory. In spin-DFT, one deals separately with the electron density $\rho^\alpha(\vec{r})$ of the spin-α electrons and the density $\rho^\beta(\vec{r})$ of the spin-β electrons, so that the exchange-correlation functional E_{XC} becomes a functional of these two quantities:

$$E_{XC} = E_{XC}[\rho^\alpha, \rho^\beta]. \tag{3.44}$$

For systems with all electrons paired, spin-DFT will reduce to ordinary DFT.

In the generalized gradient approximation (GGA) we use not only information about the density $\rho(\vec{r})$ at a particular point $\vec{r}$, but additionally the information about the gradient of the charge density. In the GGA approximation E_{XC} can be written as

$$E_{XC}^{GGA}[\rho_\alpha, \rho_\beta] = \int f(\rho_\alpha(\vec{r}), \rho_\beta(\vec{r}), \nabla\rho_\alpha(\vec{r}), \nabla\rho_\beta(\vec{r}))d\vec{r}. \tag{3.45}$$

A hybrid exchange-correlation functional mixes together the Hartree-Fock exchange term with gradient-corrected exchange and correlation terms. One of the most popular hybrid functionals is the B3LYP hybrid functional [56].

3.9 Performing Kohn-Sham density-functional calculations

The Kohn-Sham equations 3.38 can be written in a more compact form as

$$\hat{f}^{KS}\psi_i = \epsilon_i\psi_i \tag{3.46}$$

with

$$\hat{f}^{KS} = -\frac{1}{2}\nabla^2 + \left[\int \frac{\rho(\vec{r}_2)}{r_{12}}d\vec{r}_2 + V_{XC}(\vec{r}_1) - \sum_A^M \frac{Z_A}{r_{1A}}\right]. \tag{3.47}$$

Solving the Kohn-Sham equations, the orbitals ψ_i are usually expanded as

$$\psi_i = \sum_{\mu=1}^{L} c_{\mu i}\chi_\mu. \tag{3.48}$$

Inserting 3.48 into 3.47 we obtain

$$\hat{f}^{KS}(\vec{r}_1)\sum_{\nu=1}^{L} c_{\nu i}\chi_\nu(\vec{r}_1) = \epsilon_i \sum_{\nu=1}^{L} c_{\nu i}\chi_\nu(\vec{r}_1). \tag{3.49}$$

Multiplying both sides of this equation with an arbitrary basis function χ_μ and integrating over space we get

$$\sum_{\nu=1}^{L} c_{\nu i}\int \chi_\mu(\vec{r}_1)\hat{f}^{KS}(\vec{r}_1)\chi_\nu(\vec{r}_1)d\vec{r}_1 = \epsilon_i \sum_{\nu=1}^{L} c_{\nu i}\int \chi_\mu(\vec{r}_1)\chi_\nu(\vec{r}_1)d\vec{r}_1 \quad \text{for } 1 \le i \le L. \tag{3.50}$$

The integrals on both sides of this equation define the Kohn-Sham matrix

$$F^{KS}_{\mu\nu} = \int \chi_\mu(\vec{r}_1)\hat{f}^{KS}(\vec{r}_1)\chi_\nu(\vec{r}_1)d\vec{r}_1 \tag{3.51}$$

and the overlap matrix

$$S_{\mu\nu} = \int \chi_\mu(\vec{r}_1)\chi_\nu(\vec{r}_1)d\vec{r}_1. \tag{3.52}$$

Equations 3.50 can be thus written in the more compact form

$$F^{KS}C = SC\epsilon. \tag{3.53}$$

The individual elements of the Kohn-Sham matrix can be written as

$$F^{KS}_{\mu\nu} = \int \chi_\mu(\vec{r}_1)\left(-\frac{1}{2}\nabla^2 - \sum_{A}^{M}\frac{Z_A}{r_{1A}} + \int \frac{\rho(\vec{r}_2)}{r_{12}}d\vec{r}_2 + V_{XC}(\vec{r}_1)\right)\chi_\nu(\vec{r}_1)d\vec{r}_1. \tag{3.54}$$

The first two terms can be combined to one-electron integrals

$$h_{\mu\nu} = \int \chi_\mu(\vec{r}_1) \left(-\frac{1}{2}\nabla^2 - \sum_A^M \frac{Z_A}{r_{1A}} \right) \chi_\nu(\vec{r}_1) d\vec{r}_1. \tag{3.55}$$

For the third term we express the charge density according to

$$\rho(\vec{r}) = \sum_i^N |\psi_i(\vec{r})|^2 = \sum_i^N \sum_\mu^L \sum_\nu^L c_{\mu i} c_{\nu i} \chi_\mu(\vec{r}) \chi_\nu(\vec{r}). \tag{3.56}$$

The expansion coefficients are usually collected in the density matrix P with elements

$$P_{\mu\nu} = \sum_i^N c_{\mu i} c_{\nu i}. \tag{3.57}$$

The Coulomb contribution in Eq. 3.54 can be expressed as

$$J_{\mu\nu} = \sum_\lambda^L \sum_\sigma^L P_{\lambda\sigma} \int\int \chi_\mu(\vec{r}_1) \chi_\nu(\vec{r}_1) \frac{1}{r_{12}} \chi_\lambda(\vec{r}_2) \chi_\sigma(\vec{r}_2) d\vec{r}_1 d\vec{r}_2. \tag{3.58}$$

The exchange-correlation part is represented by

$$V_{\mu\nu}^{XC} = \int \chi_\mu(\vec{r}_1) V_{XC}(\vec{r}_1) \chi_\nu(\vec{r}_1) d\vec{r}_1. \tag{3.59}$$

3.10 Basis functions

3.10.1 Plane waves (PW)

Plane waves are periodic and independent of atomic positions, i.e. they are delocalized. They are a natural choice in periodic system codes such as CPMD. A plane wave (PW) orbital can be written as

$$\chi^{PW} = \sum_k c_k \exp(ik \cdot r) \tag{3.60}$$

In order to achieve the desired accuracy when using a finite PW basis set, one must choose a cutoff k_{max} which is large enough.

3.10.2 Slater-type orbitals (STO)

Slater-type orbitals (STO) seem to be the most natural choice for basis functions since they resemble the exact eigenfunctions of the hydrogen atom. A STO centered at an atom of the system under consideration is given by

$$\chi^{STO} = Nr^{n-1} \exp[-\beta r] Y_l^m(\theta, \phi). \tag{3.61}$$

N is here the normalization factor, n is the principal quantum number, β is the orbital exponent and Y_l^m are spherical harmonics functions. The problem with STOs is however that the estimation of the many-center integrals is computationally too demanding. That's why the usage of STOs is limited. A minimal basis set consists of one STO for each inner-shell and valence-shell atomic orbital of each atom. A double-zeta (DZ) basis set is obtained by replacing each STO of a minimal basis set by two STOs that differ in their orbital exponents.

3.10.3 Gaussian-type orbitals (GTO)

To speed up the calculations, one can use Gaussian-type orbitals (GTO). They are given by

$$\chi^{GTO} = Nx^i y^j z^k \exp[-\alpha r^2], \tag{3.62}$$

where N is a normalization factor and α represents the orbital exponent. $L = i + j + k$ is used to classify the GTOs as s-type(L=0) Gaussians, p-type(L=1) Gaussians, etc. Instead of using the individual Gaussian functions as basis functions, it is more common to use the so-called contracted Gaussian-type functions (CGTF), which are linear combinations of primitive Gaussian functions.

Chapter 4

Global Optimization Methods

Finding the global minimum of a high dimensional function is one of the most difficult mathematical problems. In physics, the basic challenge often consists in finding a configuration with the lowest energy, i.e. one has to minimize the energy E as a function of the M coordinates of the atoms $E(R_1, R_2, ..., R_M)$. Finding the configuration with the lowest energy is essential since it is dominant in the ensemble of configurations if the temperature is chosen low enough. We present in this chapter the mostly used algorithms for global optimization of the Born-Oppenheimer energy surface of clusters.

4.1 Overview

Finding the global minimum of the potential energy surface (PES) of a complex system is a central problem in physics, chemistry and biology. The global minimum gives the ground state configuration. At low enough temperature the system will be found in this global minimum structure assuming that this structure is kinetically accessible. For a periodic system the global minimum gives the crystalline ground state structure, for non-periodic systems it determines the geometric ground state configuration of molecules. With regard to proteins the ground state is called the native state, and the theoretical determination of this native state is one of the major challenges of modern biology. Finding the ground state of large systems is computationally very expensive and has become possible only recently. The fundamental reason why finding the global minimum is so expensive is that the number of local minima increases presumably exponentially with respect to the number of atoms in the system. Indeed, Wille and Vennik demonstrated that the problem of finding the global minimum of the PES of a cluster is NP-hard, id est the configurational complexity of this optimization increases more than polynomially with cluster size. A complete sampling of all these minima would be simply impossible for large clusters. At the beginning of a simulation the system is located in a region around

some local minimum, called basin of this local minimum. The union of several neighboring basins is called a super-basin. If one can reach from any point of a super-basin the lowest local minimum of this super-basin without crossing barriers that are very high compared to the average energy difference between the local minima, the super-basin is called a funnel (see Fig. 4.1). In a funnel landscape the local minima which are close to the global minimum are also low in energy. Realistic landscapes are multi-funnel landscapes and consist of many funnels.

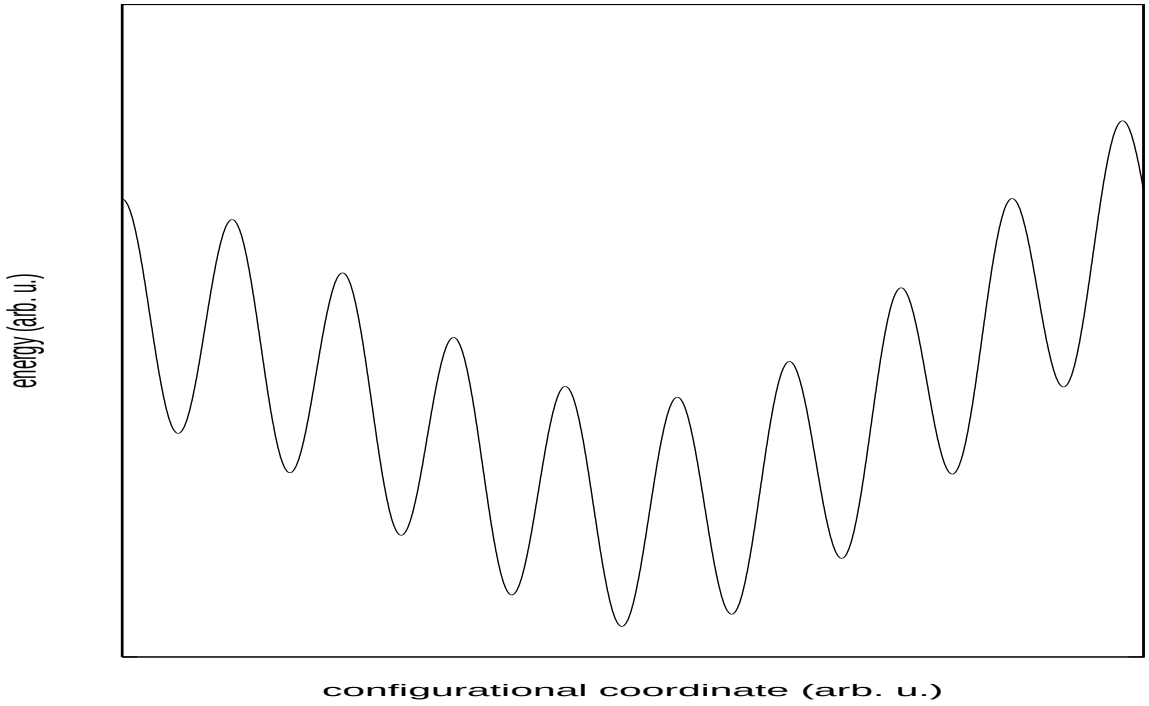

Figure 4.1: A funnel of the potential energy landscape.

Short-range potentials give rise to more local minima and to a rougher PES than soft long-range potentials. The search by global optimization can be unbiased when the starting configuration is randomly chosen, or seeded when a set of good structures is used to begin the optimization procedure. Seeded global minimum searches can be faster because they use some knowledge about the system under study, but they can also miss the true global minimum if it differs very much from the seed structure and thus lies in a different funnel. If one wants to compare the efficiency of different algorithms, one should perform unbiased searches. During the simulation one has to travel through many intermediate local minimum basins and funnels and to overcome the barriers separating the different local minima and funnels in order to reach the global minimum. The mostly used algorithms for finding the global minimum are based on thermodynamic principles, i.e. they use in some way the Boltzmann distribution

$$\frac{N_i}{N} = \frac{g_i \exp\left(-E_i/k_B T\right)}{\sum_j g_j \exp\left(-E_j/k_B T\right)} \quad , \tag{4.1}$$

where N_i is the number of molecules at equilibrium temperature T in a state i which has energy E_i and degeneracy g_i, N is the total number of molecules in the system and k_B is the Boltzmann constant. The Boltzmann distribution implies that for a non-degenerate case the probability of finding a state 1 with the energy E_1 and the probability of finding a state 2 with the energy E_2 at a given temperature T differ by the Boltzmann-factor $\exp(-(E_2 - E_1)/k_B T)$. The thermodynamic methods are usually incorporated into standard Monte Carlo technique based on the Metropolis algorithm (see Appendix A) when performing random moves or include molecular dynamics. In contrast to the thermodynamical methods, the non-thermodynamical methods such as genetic algorithms mimic the Darwinistic evolution.

4.2 Thermodynamic methods

4.2.1 Simulated annealing

Simulated annealing is based on thermodynamics and the underlying Boltzmann distribution, but takes into account the kinetic aspects. Though at a sufficiently low temperature the system should be in the ground state with the energy ϵ_0 because the probabilities of finding the system in other states with the energies ϵ_i are vanishingly small due to the Boltzmann weight $\exp(-\beta(\epsilon_i - \epsilon_0))$ with $\beta = 1/k_B T$, in practice the system will be trapped in some local minimum because at low temperature it can not overcome barriers that it has to cross in order to get into other minima. The problem can be alleviated by starting a Markov process at a high temperature and then decreasing the temperature gradually during the simulation until the system gets trapped in the ground state. This approach guarantees that the system has enough kinetic energy at the beginning to cross barriers before being trapped in the ground state. The gradual decrease of the temperature is the characteristic of simulated annealing. The two essential ingredients that characterize the simulated annealing scheme are the type of trial moves that are used and which determine the trial step probability matrix ω as well as the schedule for reducing the temperature. The simplest implementation of simulated annealing is based on molecular dynamics. Using molecular dynamics the system propagates according to the Newton's equations of motion and one does not have to come up with a prescription for the trial moves. Molecular dynamics based simulated annealing is thus imitating much faster what is happening in nature very slowly during a crystallization process. While the system is slowly cooling down, the atoms move according to Newton's law and finally may find the global minimum configuration which is the crystal structure. As in any global

optimization algorithm there is however no guarantee that the global minimum will be obtained at the end of the run.

4.2.2 Basin hopping

The basin hopping method ([10], [11]) is a canonical Monte Carlo simulation performed at constant T on the transformed PES. A basin of a local minimum is a region of attraction of this local minimum. This means that all steepest descent minimization steps that are started within the basin and which are chosen small enough will end up in this local minimum. Basin hopping is a Monte Carlo method on a modified potential energy surface. In an ordinary Monte Carlo simulation the Boltzmann factor $\exp(-(E_{new} - E_{strt})/k_B T)$ of the Metropolis step contains the energies E_{new} and E_{strt} of the new configuration X_{new} and of the starting configuration X_{strt}, which are characterized by the atomic positions $R_1, R_2, ..., R_M$. In the basin hopping method E_{new} and E_{strt} have different meanings: they are the energies of the local minima of the basins of X_{new} and X_{strt}. The hops within the basin hopping method are thus performed on a modified or transformed potential which is constant within the basin.

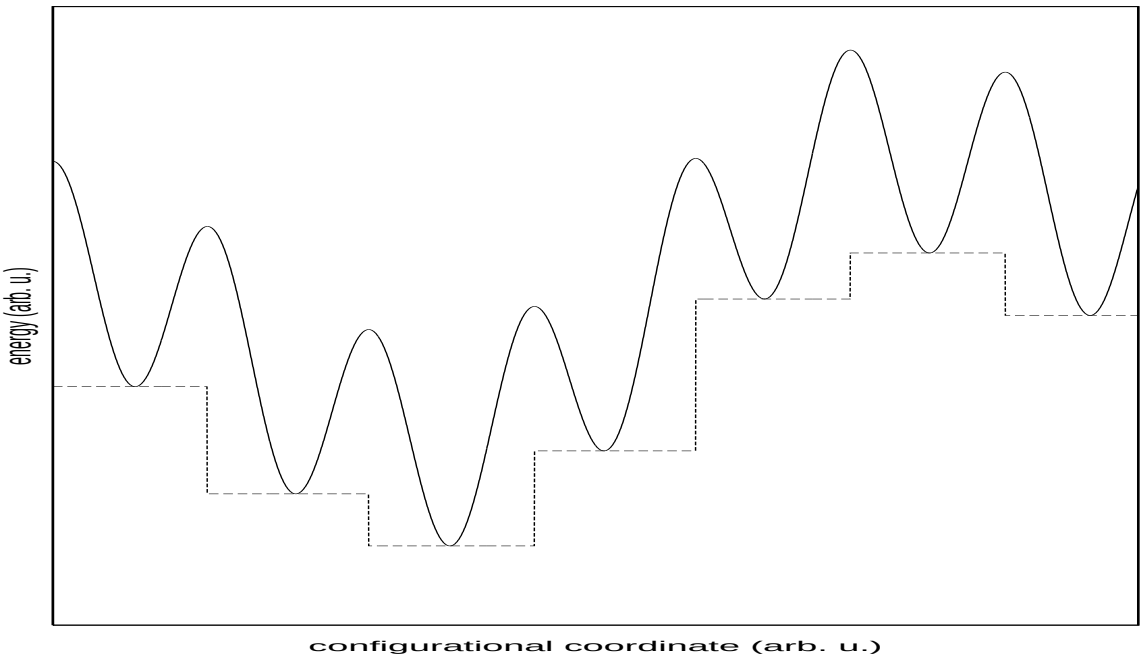

Figure 4.2: The transformed potential energy surface of the basin hopping method.

The basin hopping method offers the advantage that the barriers separating different minima can be overcome much more easily during the simulation. In an ordinary Monte

Carlo simulation the Boltzmann factor $\exp(-(E_{new} - E_{strt})/k_B T)$ can become very small when one tries to jump into another basin since the energy differences can be much larger than on the transformed potential energy surface of the basin hopping method. As a consequence jumping from one basin into another is a rather rare event in ordinary Monte Carlo simulations. Hence it can take a very long time until one finally falls into the global minimum. The calculation of the transformed potential using a local geometry optimization is performed each time a new configuration is encountered. The energy of the local minimum found in this way is then the energy which is assigned to the configuration X. The trial steps that bring us from one configuration to the next are in the simplest case just random displacements of the atoms. For small random displacements one will remain for a long time in the same basin. Since the energies do not change, all these moves are accepted in the Metropolis step. On the other hand, if one chooses very large random displacements the algorithm becomes similar to a random search. Such a random search is generally less efficient because it ignores the fact that if one has already found a good local minimum, it is likely that other even better ones are close by. A too large step size gives therefore a low acceptance probability in the Metropolis step. The step size of the random displacement is therefore usually adjusted such that half of all new configurations are accepted. There is one free parameter in the basin hopping method, namely the temperature T. Though the basin hopping method is applied to a canonical ensemble NVT where the temperature T is kept constant, T can be lowered successively during a simulation. Basin hopping can thus be used within a simulated annealing scheme, replacing the molecular dynamics. The Boltzmann-distribution guarantees us that at a sufficiently low temperature only the basin of the global minimum will be populated. But again thermodynamics can not tell us how long it will take until the thermodynamic equilibrium distribution is reached and hence how long it will take to find the global minimum.

4.3 Non-thermodynamic methods

4.3.1 Genetic algorithms

The use of genetic algorithms in cluster optimization was pioneered by Hartke [7]. The basic idea of a genetic algorithm (see for example [57]) is to follow the biological process of evolution, i.e. to mimic the Darwinistic principle of the survival of the fittest. The basic quantity in a genetic algorithm is an initial population of configurations, which is called the initial gene pool. Numerically each gene is a binary string, i.e. an integer array with each element containing 1 or 0. We can express any variable $r_i \in [0, 1]$ as

$$r_i = \frac{y_{i1}}{2} + \frac{y_{i2}}{4} + \frac{y_{i3}}{8} + \cdots = \sum_{j=1}^{\infty} \frac{y_{ij}}{2^j} \quad , \tag{4.2}$$

where y_{ij} is a decimal integer equal to either 0 or 1. We can truncate the binary string at a selected number m, whose value depends on how accurately do we want to approximate r_i. Then we can write

$$r_i \simeq \sum_{j=1}^{m} \frac{y_{ij}}{2^j}. \tag{4.3}$$

The reverse of the encoding process, id est the transformation of a binary string to a decimal number r_i, is straightforward. The initial population of the gene pool is typically created randomly. There are two issues that need to be addressed during the initialization of the gene pool. The first is the size of the population. If the population is too small, it will require more time to sample the entire possible configuration space, but if the population is too large, it takes more time to create a new generation each time. The second issue concerns the quality of the initial gene pool. If we would create all the configurations randomly, the quality of the initial gene pool would be low. Typically one first creates a number of random configurations, and then picks the best of them as ingredients of the initial gene pool. Very often, several populations are evolved in parallel, and configurations are exchanged between them from time to time.

The basic three operations performed in each generation are

1) mutation,
2) crossover and
3) selection.

A mutation consists of a random change of some bits of a gene, i.e. of a flip of one or several bits of a gene. The key element of a genetic algorithm is the concept of gene crossover. After having selected two parents genes from the parent pool, we cut each gene of the two parents at a selected point, and then join the right segment of one parent to the left segment of the other, and thus get two offsprings. An example is presented below:

1 1 0 1 1 | 0 0 0 1 0	father gene
1 0 1 0 0 | 1 1 1 1 1	mother gene
1 1 0 1 1 | 1 1 1 1 1	1.child gene
1 0 1 0 0 | 0 0 0 1 0	2.child gene

Gene crossing makes sense only if segments of a gene determine some functionalities. After having performed the operations of mutations and crossovers on a population follows the final selection or survival step. The fitness of each gene i in a population that may consist of parents and children generated by both mutations and crossovers is measured by its

fitness f_i which in a given physical problem could be for instance the negative of the energy of a configuration. The average fitness of our population $< f >$ of N individuals is given by

$$< f >= \frac{1}{N} \sum_{i=1}^{N} f_i. \tag{4.4}$$

The survival rate of gene i is proportional to $f_i / < f >$. Repeating systematically the processes of mutation, crossovers and selection gives fitter and fitter populations, and thus increases the chance that finally a population might contain the best gene, which corresponds in the mathematical language to the global maximum or minimum.

4.4 Recent developments

Recent developments when using genetic algorithms include similarity checking among cluster structures in order to keep the diversity of the population so that different funnels of the PES can be inspected as the genetic optimization goes on. Cheng [58] has proposed an effective cluster similarity checking method using the connectivity table. Configurations in different funnels of the PES differ strongly in their connectivity tables. N.Mousseau and G.T.Barkema presented 1998 [59], [60] the activation-relaxation technique (ART). An event in ART is defined as a move from a local energy minimum to another nearby minimum following a two-step process: the activation during which a configuration is pushed from a local minimum to a nearby saddle point and the relaxation that brings the configuration from this saddle point to a new local minimum. The ART technique is similar to the eigenvector-following method presented by Doye and Wales [61].

Chapter 5

Global minimum studies of silicon clusters

A large number of global minimum studies based on different algorithms has been performed for silicon clusters Si_n with $n \leq 45$ over the last 15 years. It is a well established fact that the PES of a condensed matter system can be calculated with good accuracy within DFT today, though finding the correct exchange-correlation functional remains difficult. Nevertheless, DFT methods have not been used up to now as a standard tool directly implemented in algorithms that attempt to determine the ground state of complex systems because most algorithms for the determination of the global minimum require a very large number of evaluations of the PES. Since the number of local minima of the PES of clusters scales exponentially with the number of atoms n, and each evaluation requires a full electronic structure calculation, these algorithms are computationally too demanding within the full DFT framework for silicon clusters with more than a dozen atoms. One can restrict the search of the global minimum on a subspace of the DFT-PES by using the information about the system which is studied, i.e. by performing a constrained search. In a constrained search one fixes some atomic positions or imposes some structural motifs, but experience shows that the global minimum is often missed in this way. A systematic search for the global minimum is possible with computationally less demanding approximations such as tight binding schemes and force fields. The PES of tight binding schemes and force fields differs significantly from the DFT-PES and the true PES of the system, so that the obtained global minimum candidates within these approximations are in general not the global minima within DFT. In summary, with present methods one has either the choice of using methods with a limited power of predictability or of doing a constrained search for the global minimum. To overcome this dilemma several researchers have adopted an approach where one first effectuates a systematic search with a method that allows for a fast but inaccurate calculation of the PES to obtain low-lying isomers which are global minimum candidate structures. Which of the candidate structures is lowest in energy is determined in a second step by DFT calculations. Other researchers

have combined systematic search algorithms with DFT methods, but their algorithms required too many DFT calculations to be computationally feasible if one wants to find the global minimum.

5.1 Overview

K.Raghavachari et al. [62], [63], [64], [65] have studied the structures of Si_n clusters with $2 \leq n \leq 10$ using ab initio molecular-orbital calculations. The geometries have been optimized using Hartee-Fock (HF) level of theory and Møller-Plesset perturbation theory of fourth order. The calculations have shown that clusters containing 4,6,7 and 10 atoms are particularly stable, which is consistent with experimental observations. K.M.Ho et al. [8] have obtained low energy structures of silicon clusters Si_n in the range $12 \leq n \leq 26$ by means of a genetic algorithm [66]. Their calculations have predicted the near-spherical cage structures to become the most stable for $n \geq 19$. Using the non-orthogonal density-functional tight-binding scheme (DFTB) which was proposed by Th.Frauenheim [67], A.Sieck et al. [68] have obtained low energy structures of silicon clusters Si_n with $9 \leq n \leq 14$ and have calculated their cohesive energies and HOMO-LUMO gaps. Besides, they have calculated IR and Raman spectra for the lowest energy configurations. Using simulated annealing, A.Sieck et al. [13] have addressed the shape transition by investigating Si_n clusters with 25, 29 and 35 atoms within the DFTB approach. They have found that whereas for energetically low-lying neutral silicon clusters with 25 atoms both non-spherical and spherical structures coexist, for clusters containing 29 and 35 atoms, the low energy isomers have a spherical shape. I.Rata, A.Shvartsburg et al. [9] have presented the single-parent evolution algorithm, which is a Monte Carlo like technique containing elements of a genetic algorithm. However, whereas in a standard genetic algorithm one starts with a population containing multiple parents, which are needed to perform crossover operations, the single-parent evolution algorithm involves only a single parent. Starting with some arbitrary structure, diversification operations which preserve favorable attributes are applied, and the lowest energy structure evolves in accordance with a fitness criterion. At the heart of this method are the two operations called piece reflection and piece rotation. After each of these transformations, a newly formed cluster is relaxed to the nearest local minimum, which is then defined as the offspring cluster. In accordance with the Metropolis acceptance prescription, a lower energy offspring always replaces the parent structure, while an offspring with a higher energy replaces the parent structure with a Boltzmann probability based on the energy difference between the parent and the offspring structures. Similar to the standard genetic algorithm described in the last chapter, the single-parent evolution algorithm involves a mutation operation, in which an offspring is accepted regardless of its energy. Piece reflection and piece rotation are then applied alternately in the course of the evolution of the algorithm. In order not to miss the global minimum, a new mutation cycle is started from a different part of the configuration space if the energy of the cluster does not decrease over a fixed number of

generations. The search is ended when new mutation cycles fail to decrease the energy of the cluster. Using the single-parent evolution algorithm, I.Rata et al. [9] have found a number of new low energy isomers of Si_n clusters in the range $13 \leq n \leq 23$ that can be considered as promising global minimum candidates. Recently, K.A.Jackson et al. [14] have systematically studied the prolate-to-spherical shape transition of Si_n clusters in the range $20 \leq n \leq 27$ using the DFTB scheme and a new "big bang" optimization method. The essence of the "big bang" optimization method is to create random configurations of n atoms and to relax them to a local minimum using the DFTB scheme and a standard gradient-based algorithm. Millions of such minima are generated for each n by starting from different random geometries thus allowing all possible shapes to emerge. For each cluster size, 200-400 of the best DFTB local minima are selected for investigation by DFT. K.Jackson et al. [14] have suggested in their study that whereas for Si_n clusters with $n \leq 19$ the low energy structures consisting of extremely stable Si_6 octahedron and Si_9 tricapped trigonal prism (TTP) [8] subunits assume the prolate form, the low energy structures for silicon clusters with $n \geq 20$ assume the minimum-surface spherical shapes. J.Grossmann et al. [69], [70] have performed QMC calculations for Si_n clusters in the range $2 \leq n \leq 20$. J.Jeong et al. [71] have performed LDA calculations for Si_n clusters in the range $9 \leq n \leq 14$ and QMC calculations for several low energy Si_{13} isomers. Röthlisberger et al. [12] have used simulated annealing within DFT to find structural motifs of the medium-sized silicon clusters. They have obtained their final lowest energy geometries for Si_{45} by an iterative annealing process involving symmetry constraints on the candidate structures and a subsequent extensive relaxation free of symmetry constraints. Recently, A.Tekin and B.Hartke [4] have obtained new global minimum candidates for Si_{11}, Si_{13}, Si_{14} and Si_{15} clusters. Yoo and Zeng [72] were the first researchers to conduct systematic search for the global minimum on the DFT-PES. They have combined basin-hopping (BH) with DFT and have performed a systematic BH search within DFT for silicon clusters Si_n with $12 \leq n \leq 16$. By this means they have found a new global minimum candidate structure for Si_{16}. For larger clusters they have performed constrained search and have found new global minimum candidates for Si_{17}, Si_{18} and Si_{22}. However, though the same lowest-energy structure of Si_{16} could be obtained with systematic DFT-BH regardless of the initial structure within less than 5000 Monte Carlo trials, the systematic DFT-BH has started to show dependence on the initial structure starting from Si_{17}. A systematic DFT-BH is therefore computationally too demanding to be feasible for larger cluster within acceptable amount of time.

Chapter 6

The Dual Minima Hopping Method

We present a new method, which is based on the minima hopping method (MHM) [16] and which we shall refer to as the dual minima hopping method (DMHM). This method allows us to find the global minimum of the potential energy surface (PES) within density functional theory (DFT) for systems where a fast but less accurate calculation of the PES is possible. This method is not based on thermodynamics and can rapidly find the ground state configuration of clusters and other complex systems with present day computer power by performing a systematic search. We apply the new method to silicon clusters Si_n in the range $16 \leq n \leq 19$. Even though these systems have already been extensively studied by other methods, we find new global minimum candidates within PBE for Si_{16} and Si_{19} as well as new low-lying isomers for Si_{16}, Si_{17} and Si_{18}.

6.1 The Bell-Evans-Polanyi principle

The Bell-Evans-Polanyi (BEP) principle comes from chemistry and states that highly exothermic chemical reactions have a low activation energy. According to the BEP principle, within a series of closely related reactions one can sometimes observe a linear relation between the energy of activation E_a and the enthalpy of reaction ΔH_r:

$$E_a = A + B\Delta H_r. \tag{6.1}$$

Marcus theory even states that the dependence of the activation energy on the enthalpy is parabolic. The fundamental assumption of Marcus theory is that the potential energy landscape along the reaction path can be approximated by two parabolas centered at the two local minima. The BEP principle is demonstrated in Fig.6.1. In the context of global

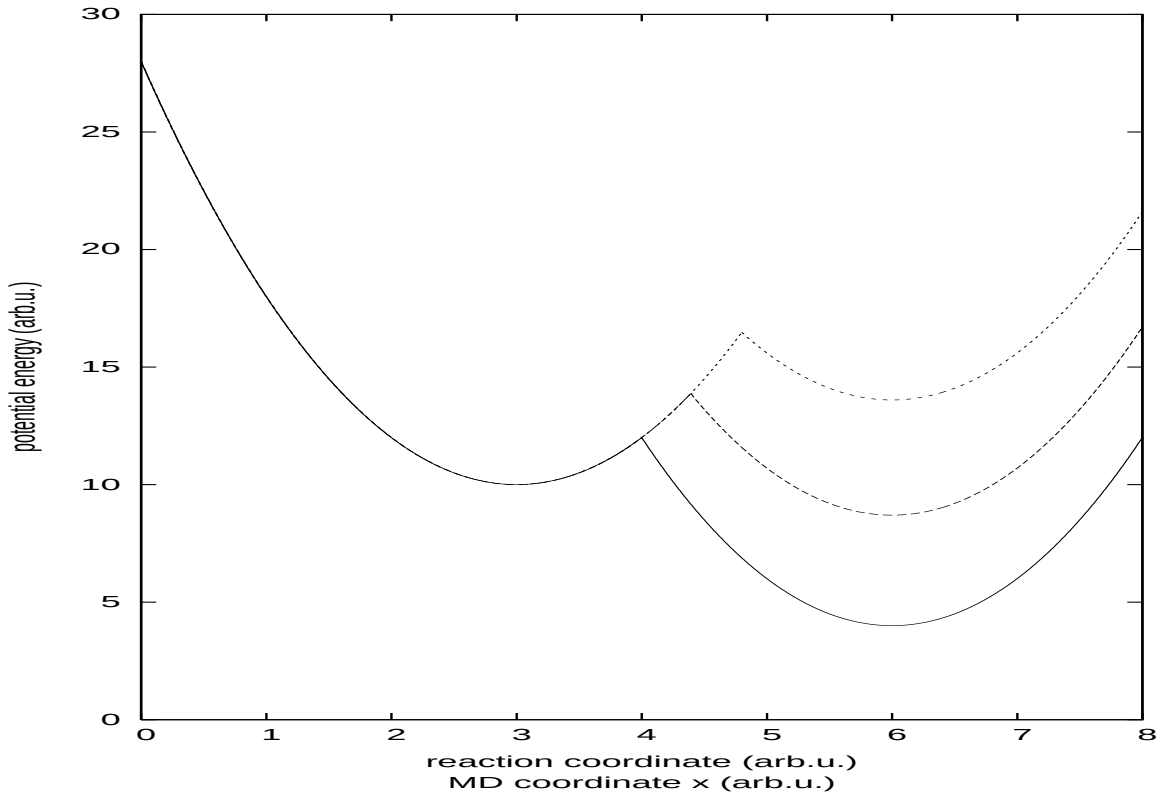

Figure 6.1: The illustration of the BEP principle in the context of Marcus theory. Higher lying parabolas correspond both to higher activation energies and higher energies of the new local minimum.

minimum search on the Born-Oppenheimer surface the BEP principle implies that one is more likely to find a low energy local minimum by crossing from the current basin into a new basin over a low energy barrier than over a high energy barrier. It is especially true in the context of global optimization as compared to a single chemical reaction or a single hop from one basin into another because it has to hold only in an average sense and not for each individual barrier crossing. However, it should be pointed out that whereas the BEP principle is a statement about the true physical transition state, it means something different in the context of global optimization where one usually crosses energy barriers in the molecular dynamics escape step which are much higher than those of the exact physical transition state. We will therefore refer to it as molecular dynamics BEP, or abbreviated MDBEP. The high kinetic energies in the molecular dynamics escape step are necessary in order to prevent the system from being trapped in the initial local minimum since it is not easy to find the exact transition state.

6.2 The shortcomings of existing global optimization methods

Except for genetic algorithms, the predominantly used global optimization methods are based on thermodynamics. Thermodynamic methods such as simulated annealing or basin hopping aim to achieve the Boltzmann distribution. However, it is very difficult to estimate the number of steps which is needed in order to find the global minimum when using thermodynamic methods since the same regions of configurational space will be visited several times. It is possible that the method will jump back and forth between two configurations for a very long time. In a multifunnel landscape the system can be easily trapped in a wrong funnel and the global minimum will be missed in this way. The choice of temperature or temperature scheme is of crucial importance for the performance of the thermodynamic methods and can't be known a priori. Besides, thermodynamic principles do not take into account the MDBEP principle. They are consequently of limited value. Genetic algorithms can be very powerful and have been indeed successfully applied to silicon clusters. Unfortunately, they allow only a constrained search since they cover only a subspace of the total configurational space and prefer in general some structural motifs, which are only slightly modified by the mutation and crossover operations. An unconstrained non-thermodynamic systematic search method which avoids revisiting of old configurations would be very helpful in this context. The problem of repeated visits of configurations has already been addressed by some researchers. One idea that was proposed is flooding [73], [74]. The principle of flooding is that in basins that were already visited during the simulation, the potential is lifted and it is less likely that a configuration in the same region of configuration space will be accepted in a future Monte Carlo step. Another version of flooding [75] is done not in the high dimensional configurational space, but in a low dimensional space spanned by suitably defined parameters of the system. The problem with flooding is that it is difficult to determine the boundaries of the basin which should be flooded. Another problem with flooding is that the flooding of presumable transition basins between different funnels may significantly deteriorate the performance of the algorithm.

6.3 The minima hopping method (MHM)

Recently, Stefan Goedecker has proposed a novel method, the Minima Hopping Method (MHM) [16]. It avoids revisiting of old configurations, is not based on flooding and takes into account the MDBEP principle. The MHM algorithm has a double loop structure: in the inner loop one attempts to escape from the current local minimum, in the outer loop one accepts or rejects new local minima found by successful escape attempts. A *history* list keeps track of all minima found. Introducing a history list makes the simulation non-Markovian. A feedback mechanism uses information from this history list to make

more vigorous escape attempts when the algorithm is revisiting previously found minima thereby preventing the algorithm from getting trapped in an incorrect minimum. The escape step is done by a short molecular dynamics simulation that starts from the current minimum followed by a geometry relaxation. The geometry relaxation is done by a combination of steepest descent and conjugate gradient methods. The atoms get a randomly created Maxwell-Boltzmann velocity distribution such that their kinetic energy is equal to $E_{kinetic}$. The molecular dynamics escape step is then performed for a microcanonical ensemble (N,V,E_{kin}). The system with the kinetic energy $E_{kinetic}$ has sufficient energy to cross over a barrier of height less than $E_{kinetic}$ relative to the energy of the current local minimum. The kinetic energy is reduced during the molecular dynamics simulation by the height of the interatomic potential E_{pot}. The molecular dynamics simulation is stopped as soon as the potential energy has crossed *mdmin* maxima along the trajectory. Subsequently, the geometry relaxation starts. If $E_{kinetic}$ is small, one will usually fall back into the current minimum, if it is big, one will land in most cases in a different minimum. However, due to the MDBEP principle, escapes with large $E_{kinetic}$ will in general lead to high-lying local minima, whereas the preference in an escape step should be given to energetically low-lying configurations. The MHM algorithm is shown below.

The minima hopping method (MHM) algorithm:

initialize a current minimum 'M$_{current}$'
ESCAPE TRIAL PART

MDstart: start a MD trajectory with kinetic energy E$_{kinetic}$ from current minimum 'M$_{current}$'
Once potential energy reaches another minimum along the trajectory, stop MD and optimize geometry to find the closest local minimum 'M'
if ('M' equals 'M$_{current}$') then
E$_{kinetic}$ = E$_{kinetic}$*β_1 ($\beta_1 > 1$)
goto MDstart
else if ('M' equals a minimum visited previously) then
E$_{kinetic}$ = E$_{kinetic}$*β_2 ($\beta_2 > 1$)
else if ('M' equals a new minimum) then
E$_{kinetic}$ = E$_{kinetic}$*β_3 ($\beta_3 < 1$)
endif

DOWNWARD PREFERENCE PART

if (energy('M') - energy('M$_{current}$') < E$_{diff}$) then
accept new minimum: 'M$_{current}$' = 'M'
add 'M$_{current}$' to history list

E_{diff} = E_{diff}*α_1 ($\alpha_1 < 1$)
else if rejected
E_{diff} = E_{diff}*α_2 ($\alpha_2 > 1$)
endif

goto MDstart

Three cases can be distinguished after a molecular dynamics escape step with subsequent geometry relaxation. In the first case the geometry relaxation will lead back to the initial local minimum that was used as the starting point. The kinetic energy $E_{kinetic}$ is then increased by a factor β_1 and a new molecular dynamics trajectory is started. By choosing β_1 very close to 1 and by increasing the kinetic energy $E_{kinetic}$ only slightly, one can take into account the MDBEP principle. In the second case the geometry relaxation leads to a local minimum that has already been visited during the simulation and has already been added to the history list after it was accepted in the outer acceptance/rejection loop. Subsequently, the kinetic energy $E_{kinetic}$ is increased by a factor β_2. The kinetic energy $E_{kinetic}$ is increased in the first two cases in order to enable a crossing into a new unexplored region of the configurational space and to enable a successful molecular dynamics escape step. In the third case the geometry relaxation leads to a new local minimum. This is the most desirable case since exploration of new configurations may lead to the global minimum. The kinetic energy $E_{kinetic}$ is decreased in such a case by a multiplication with the factor factor β_3 which is smaller than 1. This prevents the system from exploding before the configurational space has been thoroughly explored, and guarantees that the configurational space around the new local minimum will be first explored with a kinetic energy $E_{kinetic}$ which is not too large. Keeping track of all the visited local minima of the PES of silicon clusters requires some identification criterion. In the context of force field or tight binding calculations, the identification of clusters is an easy task, since the energy of a local minimum configuration can be determined with very high accuracy in this context. It is therefore enough simply to store the energy of each new configuration that is accepted in order to be able to identify it later.
The acceptance/rejection of the new local minimum is done by simple thresholding. A configuration is accepted if the energy of a new local minimum with energy E_{new} rises by less than E_{diff} as compared to the current energy E_{curr}. α_1 and α_2 determine how rapidly E_{diff} is increased or decreased in the case that a new configuration is rejected respectively accepted. Half of the moves is accepted and half of the moves is rejected if α_1 and α_2 are chosen such that $\alpha_1\alpha_2 = 1$. After the system has explored low energy regions of the PES, it starts to explore higher energy regions. This is due to the fact that $E_{kinetic}$ is increased each time whenever a known configuration is revisited. Once $E_{kinetic}$ becomes very large, the simulation should be stopped because otherwise the system will explode.

6.4 The verification of the MDBEP principle with the MHM method

Using the MHM method, we have verified the MDBEP principle for 3 different systems: Lennard-Jones cluster of 38 atoms, Lenosky force field Si33 cluster and Lenosky tight binding Si20 cluster. The results are presented in Fig. 6.2, Fig. 6.3 and Fig. 6.4. For each system we have first chosen a sequence of kinetic energies in some reasonable interval, each of these kinetic energies is a data point in the corresponding Figures. For each fixed kinetic energy we have performed 100 runs using the MHM method in order to get good statistics and have then calculated the average number of local minima visited before the global minimum was found. As one can see in Fig. 6.2, Fig. 6.3 and Fig. 6.4, one finds the global minimum much faster when E_{kin} is small. This observation is an indirect confirmation of the MDBEP principle.

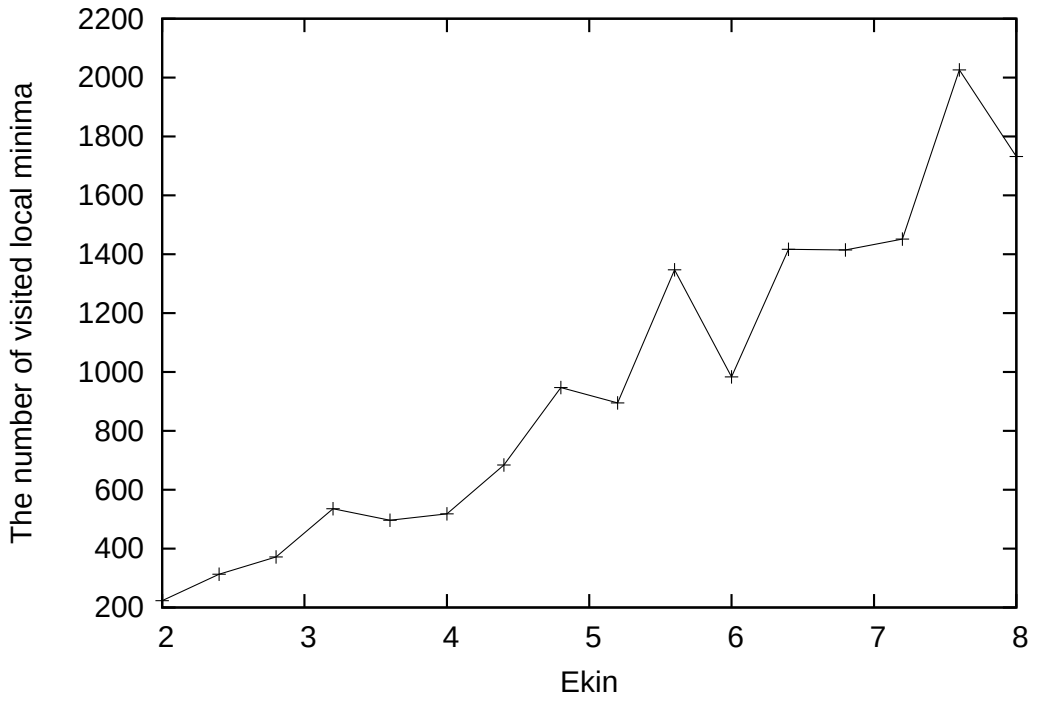

Figure 6.2: The MDBEP principle for the Lennard-Jones cluster of 38 atoms

6.5 The Dual Minima Hopping Method (DMHM)

In the ordinary version of the MHM [16] the forces for the MD and for the geometry optimization part are done with the same method. Fast methods such as force field or tight

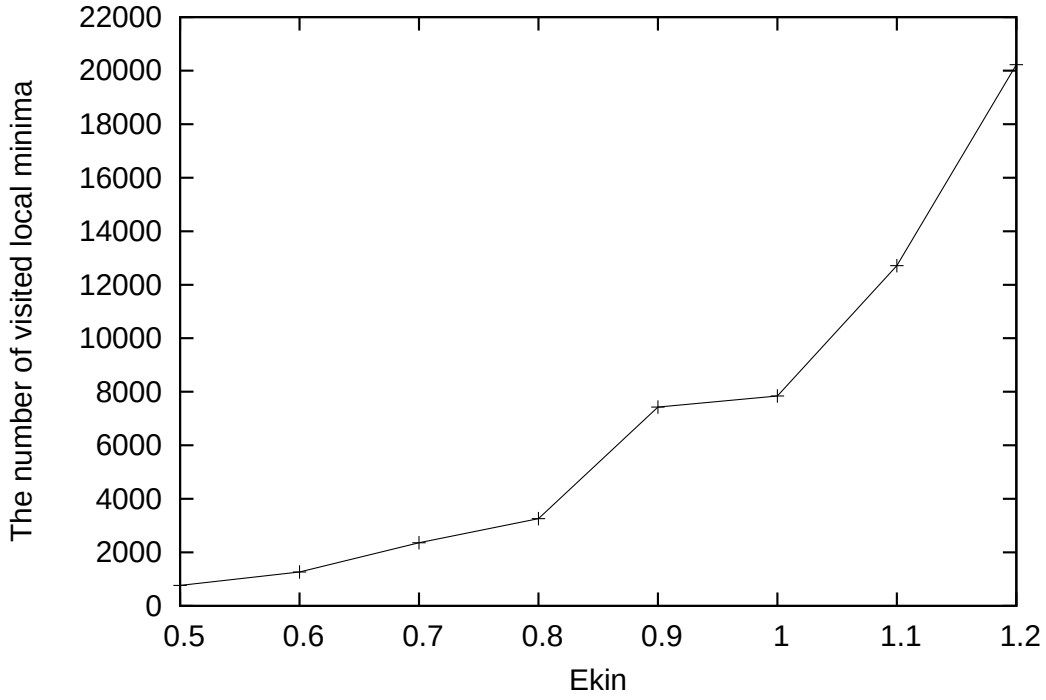

Figure 6.3: The MDBEP principle for the Lenosky force field Si33 cluster

binding methods have to be used to limit the computing time to an acceptable length. In the method presented in this dissertation two different methods are combined: a slow but accurate method and a fast but less accurate method. The fast method is used for the MD part and for the first few steps of the geometry optimization. The accurate method is then used for the final geometry optimization and the evaluation of the energy of the relaxed structure. In this way the search for the global minimum is reduced to a relatively small number of geometry optimizations with the accurate and expensive method plus a much larger number of force evaluations with the fast method. Henceforth, we shall refer to this modified minima hopping algorithm, that combines the two methods for the calculation of the forces, as the dual minima hopping method (DMHM).
The fact that the input configuration for the geometry optimization with the accurate method is a configuration that was prerelaxed with the fast method is important for the stability of the entire algorithm if the accurate method is a DFT method. DFT programs do typically not converge if the input configuration is far from any physically reasonable configuration. The prerelaxation with the fast method excludes the possibility that a physically unreasonable state is used as an input configuration. From the previous considerations it might seem advantageous to do a full prerelaxation, i.e. to use a local minimum of the fast method as the input for the geometry optimization with the accurate method. If the fast method is a reasonable approximation then a local minimum found by it will often be close to a local minimum of the accurate method.

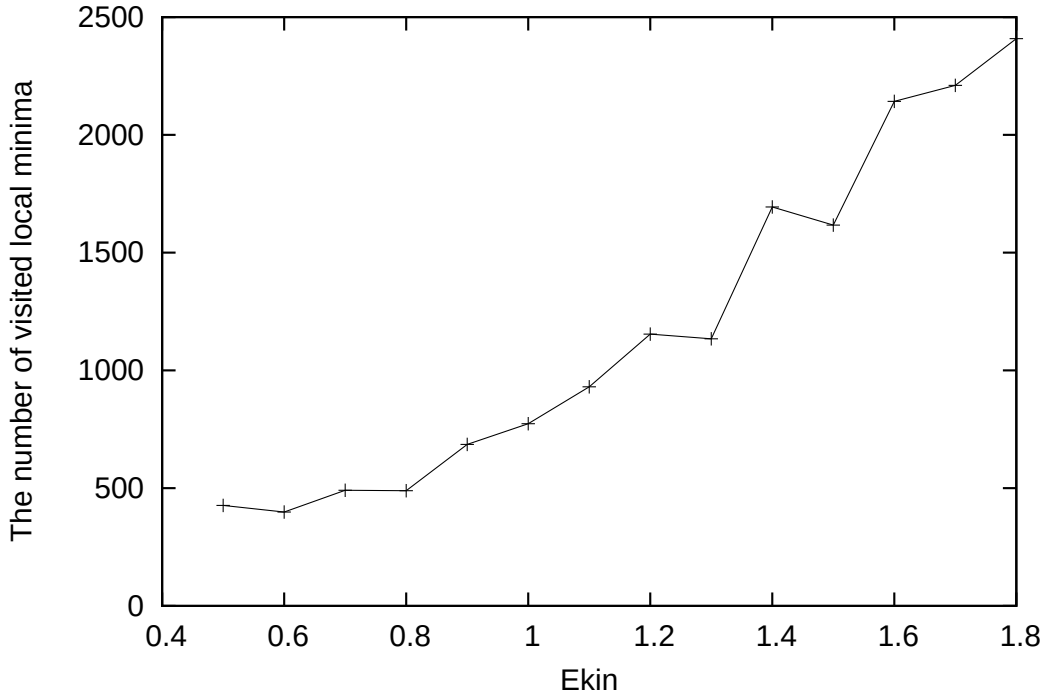

Figure 6.4: The MDBEP principle for the Lenosky tight binding Si20 cluster

Unfortunately, in general there is no one-to-one correspondence between minima obtained from the two methods. Therefore, some local minima obtained using the accurate method are inaccessible from the starting configurations provided by the fast method. For this reason only a small number of steps should be done in the prerelaxation with the fast method. In this way the ensemble of the starting configurations for the geometry optimization with the accurate method comprises a considerable part of the configurational space (and not only the ensemble of all the minima of the fast method) and one can reach virtually any minimum of the accurate method. The MDBEP principle is essential for the success of the MHM as has been shown in [16]. The correlation between the barrier height and the energy of the minimum 'behind' the barrier certainly deteriorates if one is combining two different methods. This implies more local minima will be visited, on average, with the DMHM before the global minimum is found than with the ordinary MHM. In order to explore the influence of this reduced correlation we did systematic tests with a 38 atom Lennard-Jones (LJ) cluster. This is a system for which the global minimum is hard to find since it is contained in a small secondary funnel [76], [11], [77] but the computing time is small since the potential can be evaluated very rapidly. As the accurate method we used the LJ potential. As the 'fast' method we used a truncated polynomial approximation of the LJ potential as shown in Fig. 6.5. As expected, the number of local minima that are visited on average before the global minimum is found increases from 380 to 530, nevertheless, the number of force evaluations needed with the

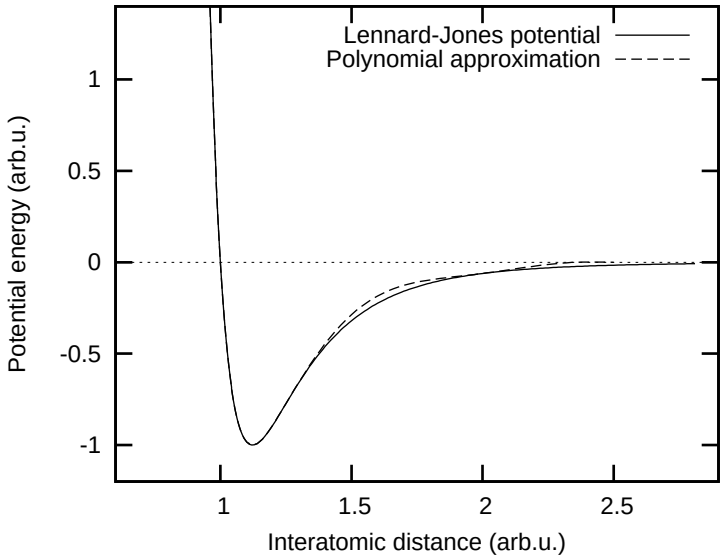

Figure 6.5: The truncated polynomial approximation of the LJ potential and the exact LJ potential.

'expensive' exact LJ method is reduced by a factor of 5.
To demonstrate that the DMHM can indeed find the global ground state geometry of real clusters, we have applied it to silicon clusters. Numerous groups are involved in the search of the ground state of silicon clusters and there are at least 50 theoretical papers on this subject [12], [72], [5], [8], [78], [79], [80], [81], [82], [9], [14], [4], [83], [84]. Applying DMHM to silicon clusters we were able to find all of the known structures [79], [80], [81], [82] in the range Si_4-Si_{19} and we even found lower energy structures for Si_{16} and Si_{19} in spite of the fact that silicon clusters up to 19 atoms in size have already been extensively studied. The new global minimum structures within CPMD/PBE (see below) Si_{16a} and Si_{19a} as well as the new low-lying isomers Si_{16b}, Si_{17a}, Si_{17b} and Si_{18a} are shown in Fig. 7.2. The structure Si_{16a} contains the TTP-Si_9-subunit [85] and is compact in contrary to the structure Si_{16} reported by X.C.Zeng [5]. The structure Si_{19a} consists of a TTP-Si_9-subunit and a Si_{10}-subunit. The low-lying isomer Si_{16b} is compact and highly symmetric. The low-lying isomer Si_{17a} consists of a TTP-Si_9-subunit and a Si_8-subunit. The low-lying isomer Si_{17b} consists of two equal 7-blocks, which are rotated against each other, and a triangle as a cleaving block. The low-lying isomer Si_{18a} is prolate and consists of two TTP-Si_9-subunits which are rotated against each other. In contrast to the previous works, the new configurations as well as the putative global minimum structures reported previously were found by the DMHM automatically after having visited only a few hundred local minima. As the fast method we have used the Lenosky tight binding scheme for silicon [17]. As the accurate method we have tested three different DFT codes: all-electron DMOL code [87], [88], pseudopotential based CPMD code [89] and pseudopotential based Quickstep code [90]. Unfortunately, the DMOL and CPMD codes were to

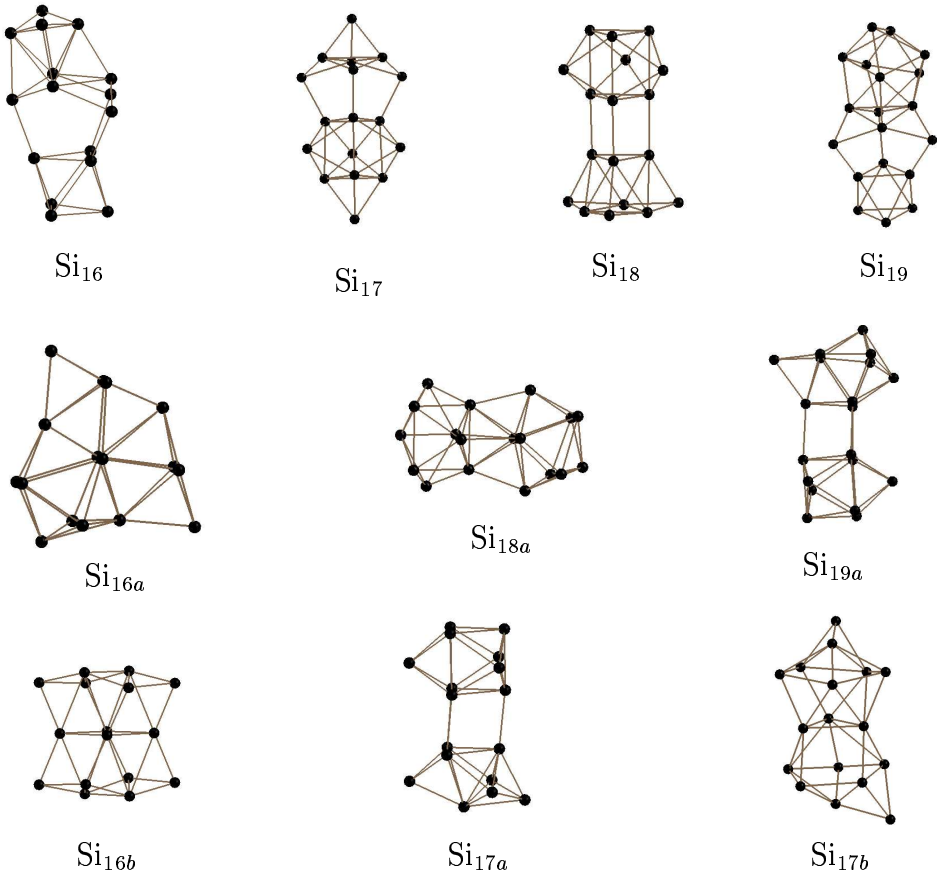

Figure 6.6: New low energy geometries Si_{16a}, Si_{16b}, Si_{17a}, Si_{17b}, Si_{18a} and Si_{19a} found in this work with DMHM and the putative global minimum structures Si_{16} [5], Si_{17} [8], Si_{18} [8] and Si_{19} [9] reported previously and reproduced by the DMHM. The new geometries will be posted on the Cambridge Cluster Database [86].

slow in order to be implemented in the DMHM. The accurate method as implemented in the DMHM is therefore the Quickstep code [90]. After having performed the DMHM with Quickstep using a relatively small Gaussian basis set and the local density approximation (LDA), we have calculated accurate final energies and zero-point energies with the CPMD program [89] using the PBE functional [91], a high accuracy pseudo-potential [92], large super-cells (24 Å) and a sufficient plane wave cutoff (28 Rydberg). The results for Si_{16a}, Si_{16b}, Si_{17a}, Si_{17b}, Si_{18a} and Si_{19a} as compared to Si_{16}, Si_{17}, Si_{18} and Si_{19} (see Fig. 7.2) are presented in Table 6.1. A comparison to the new low-lying isomers (not presented here) Si_{17} and Si_{18} found by Zeng *et al.* in [5] should also be made. The isomer Si_{17a} is lower by 0.16 eV, the isomer Si_{17b} is lower by 0.06 eV within CPMD/PBE than the low-lying Si_{17} isomer reported by X.C.Zeng [5]. The Si_{17} structure reported by Ho *et al.* in [8] is however 0.09 eV lower than our isomer Si_{17a}. The isomer Si_{18a} is lower by 0.28 eV than the low-lying Si_{18} isomer reported by X.C.Zeng [5]. In contrast to other

Cluster	Si_{16a}	Si_{16b}	Si_{17a}	Si_{17b}	Si_{18a}	Si_{19a}
PBE	-0.15	0.02	0.08	0.20	0.24	-0.08
PBE(Z)	-0.16	0.01	0.09	0.23	0.19	-0.09

Table 6.1: The energy differences in eV without and with zero-point energy correction between the new low energy geometries Si_{16a}, Si_{16b}, Si_{17a}, Si_{17b}, Si_{18a} and Si_{19a} found in this work with DMHM and the putative global minimum structures Si_{16} [5], Si_{17} [8], Si_{18} [8] and Si_{19} [9] reported previously using the PBE exchange-correlation functional as implemented in CPMD.

exchange correlation functionals, the PBE functional [91] was not fitted to any chemical systems with simple bond structures and is expected to give the most accurate description of the complex bonding patterns found in silicon clusters. The term 'accurate' must be handled with caution however, since DFT is only an approximation and, as a matter of fact, the energetic ordering may change if one uses different functionals [82]. Among the various force fields and tight binding schemes that exist, we have tested systematically the Lenosky force field [93] and the Lenosky tight binding scheme [17]. The correlation between Lenosky force field energies and density functional energies for various configurations of a Si_{25} cluster is very bad as one can see in Fig. 6.7. The Lenosky tight binding scheme [17] gave a very good agreement with the DFT energies. It can predict the DFT energies with an error of roughly 1 eV as shown in Fig. 6.8. Fig. 6.8 also shows why the common approach of first finding candidate structures by doing a systematic search with a cheap method and then checking by an accurate method which of the candidate structures gives the global minimum is problematic except for very small systems. For a 25 atom silicon cluster the number of geometric configurations within 1 eV above the ground state is of the order of 10^4 states, for a 33 atom cluster it is already of the order of 10^5 states and it increases exponentially with system size. It is therefore virtually impossible to check which out of these 10^4 to 10^5 configurations is the global minimum within DFT. Besides, because of the absence of the one-to-one correspondence between the local minima of the fast method and of the accurate method, it is not guaranteed that any of the minima of the fast method will lead to the global minimum of the accurate method upon relaxation.

The identification of the previously visited minima is an essential ingredient of the MHM. In the context of the ordinary MHM the energy can be used to identify configurations since it is possible to calculate the energy with many significant digits both for force fields and tight binding schemes. With DFT programs this is not any more possible because of the presence of numerical noise. For this reason we have used in addition to the DFT energy all inter-atomic distances. Two DFT minima are considered to be identical if all their inter-atomic distances ordered by magnitude agree to within a certain tolerance. Another possibility of identifying the DFT cluster geometries when using a tight binding scheme as fast method is the back relaxation from the DFT geometry to the tight binding (TB) geometry and the subsequent identification based only on the TB energy, just as in the ordinary MHM.

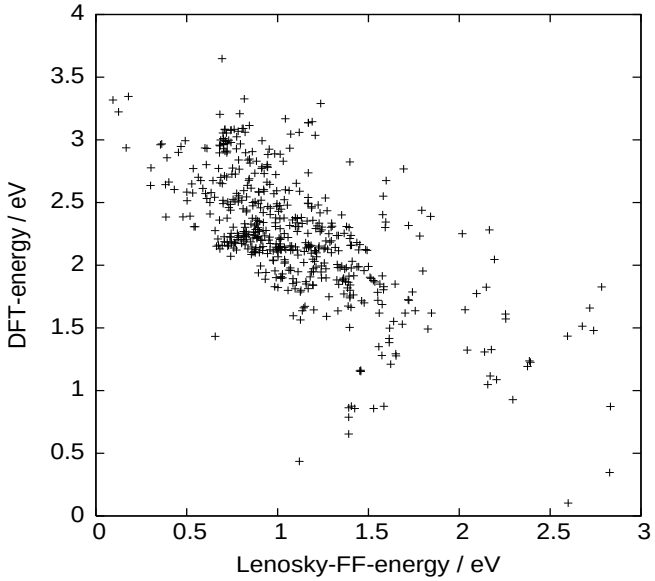

Figure 6.7: The correlation between force field and density functional energies for various configurations of a Si_{25} cluster. The scattering shows that force field energies do not correlate with density functional energies: larger force field energies correspond to smaller density functional energies and vice versa.

6.6 Summary

We have presented a method that allows one to find the global minimum of the DFT potential energy surface within acceptable computer time for moderately complex systems. The method is efficient for the following reasons. First, it requires only DFT calculations for configurations where DFT programs typically converge without problems. It does not, for instance, require DFT calculations for configurations generated by random displacements from a previous configuration. Second, the MHM is highly efficient in the sense that the number of minima visited before the ground state is found is small. Even though the DMHM is not quite as good from this perspective it is still efficient if the fast method used for the MD part is qualitatively correct. Third, most of the force evaluations are done with the fast method and the total effort for finding the global minimum is equal to the effort of doing only a computationally affordable number of geometry optimizations with the accurate method.

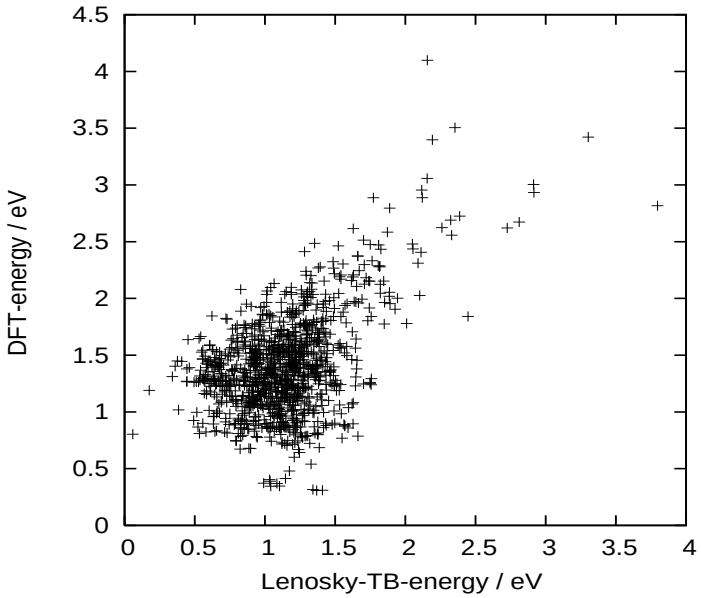

Figure 6.8: The correlation between tight binding and density functional energies for various configurations of a Si_{25} cluster. If the correlation was perfect all the points would lie on the diagonal. Instead the scattering shows that the tight binding energies can predict the energy differences between various cluster configurations only with an error of about 1 eV.

Chapter 7

Coexistence of low-lying isomers for medium-sized Si clusters

We challenge the existence of a unique geometric ground state structure for certain Si clusters by performing DFT calculations. We show on the basis of the DFT calculations that for Si clusters with up to 19 atoms the lowest ten isomers coexist within a tiny energy interval. Only Quantum Monte Carlo (QMC) calculations can thus provide reliable energies for the best global minimum candidates. On the basis of the QMC calculations performed for a number of clusters by Richard Hennig we conclude that for some clusters the energy differences are so small that entropy effects can change the energetic ordering of the configurations. In particular, configurations with rotational symmetry consisting only of ^{28}Si isotopes and symmetric configurations containing one ^{29}Si isotope are disfavored by these effects. Comparisons with experiment are thus difficult since a mixture of several configurations is to be expected at thermal equilibrium.

7.1 Introduction

The determination of the structure of clusters is a difficult task since the main source of experimental information, ion mobility measurements [94], gives only crude information about the overall shape of a cluster. The exact atomic positions of all the atoms forming the cluster remain unknown. For this reason computational simulation is an interesting alternative to the experimental approach, which has been widely used for silicon clusters. From the theoretical point of view the ground state structure of a solid state system is determined by the global minimum of the Born-Oppenheimer potential energy surface (PES). Finding the global minimum using computational simulation requires global optimization algorithms. Two problems arise in this context. First, most global optimization algorithms give no guarantee for finding the global minimum within a finite amount of

computer time. Second, the Born-Oppenheimer PES has to be calculated with very high precision.
Concerning the first point there is now a large amount of agreement between different methods for medium-sized clusters containing up to 19 atoms [81], [82]. Genetic algorithms [7], [8], [9], the big-bang method [14], the basin hopping method [95], [96], [5] and the minima hopping method [16] give typically similar or even identical results. The discrepancies are rather due to the different exchange-correlation functionals that were used in different investigations [6].
The existence of a well defined ground state structure is generally taken to be granted for silicon clusters. Silicon clusters are however very different from bulk silicon where the second lowest configuration (a fourfold coordinated defect [97]) is 2.4 eV higher than the crystalline ground state. Clusters are frustrated systems, where most of the atoms can not adopt their favorite fourfold coordination [98]. This can lead to small energy differences between different configurations. The significant deviations of the clusters bond lengths from the crystalline bond lengths shown in Fig.7.1 illustrate this frustration.

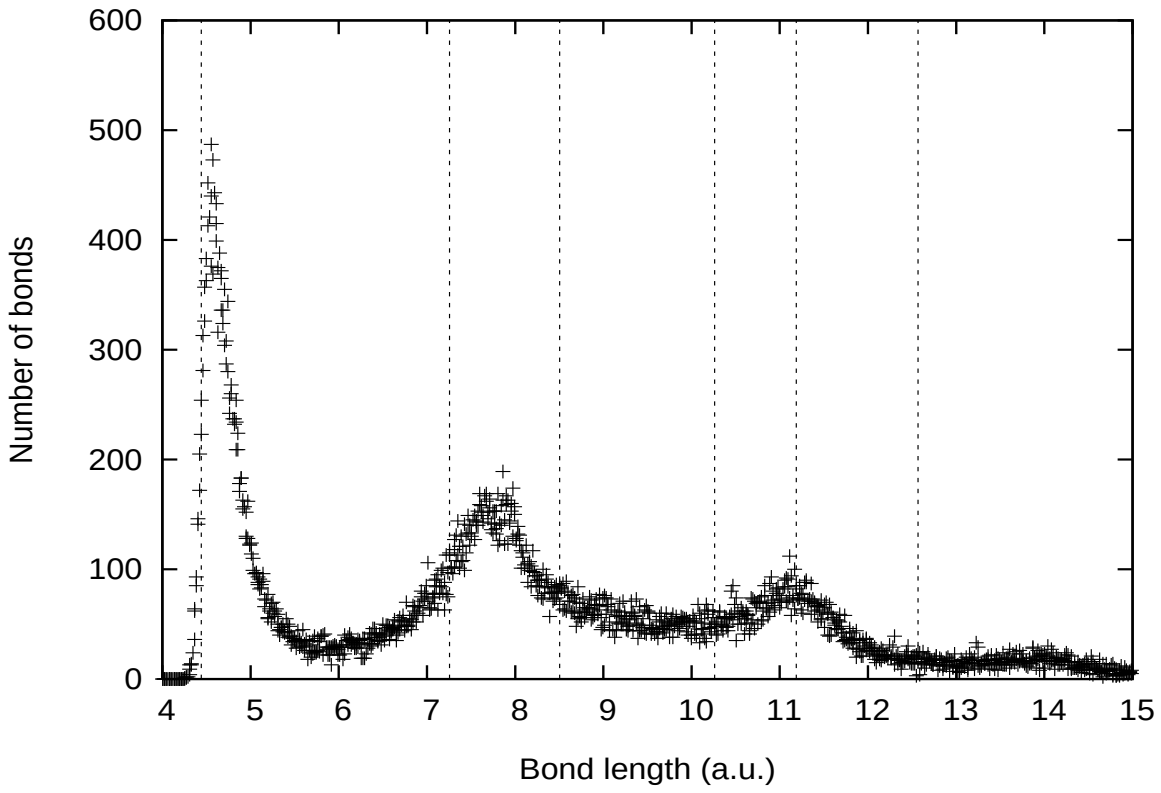

Figure 7.1: The bond length distribution averaged over various low-lying Si17-configurations. The six vertical lines indicate the 1st to 6th nearest neighbor distances in the crystal.

7.2 Configurational energies of the 10 lowest lying isomers

In our research work work we did not only search for the ground state configuration of silicon clusters with up to 19 atoms, but for a large number of low energy configurations. This is possible with the dual minima hopping method (DMHM) [99], which has the property that it explores higher and higher energy configurations after having found the global minimum. We have applied the DMHM using the QUICKSTEP code with LDA as exchange correlation functional to silicon clusters Si_n in the range $7 \leq n \leq 19$. In this size range we have found and stored between 15 different low energy isomers for Si_7 and more than 10000 different isomers for Si_{19}. Since the LDA exchange correlation functional is not reliable, we have subsequently performed geometry relaxation for the lowest 50 LDA/QUICKSTEP configurations using the DMOL code and PBE exchange correlation functional. Though the DMOL code offers the advantage of having fast geometry optimizer, its output energies differ slightly from those of CPMD and Gaussian as we shall see later. For this reason we have performed in the final step a wavefunction optimization for the PBE/DMOL geometries using the CPMD code with PBE exchange correlation functional. The energies of the 10 lowest PBE/CPMD configurations of silicon clusters containing 7 to 19 atoms that were obtained in this way are presented in Table 7.1, the geometries of the corresponding configurations are presented in Appendix D. The energy difference between the global minimum and the second lowest minimum is 0.8 mHa for Si_{11}, 0.9 mHa for Si_{13}, 2.1 mHa for Si_{14}, 3.1 mHa for Si_{17} and 3.2 mHa for Si_{19}. Fig. 7.2 shows the first major result of our investigation, the energies of the 10 lowest configurations of silicon clusters within PBE containing 7 to 19 atoms, graphically. Apparently, with larger cluster size the energy interval for the 10 lowest configurations decreases strongly. For both Si_{13} and Si_{17} the 10 lowest configurations are in an interval of roughly 10 mHa. Since room temperature corresponds to $\sim$1mHa, entropy effects can and actually will play an important role for certain clusters.

7.3 The choice of the basis set

In order to be able to compare the PBE energies when using 3 different codes, DMOL, CPMD and Gaussian, we must first choose for each code an appropriate basis which should be large enough. We have taken structures that were obtained by R. Hennig through symmetrization using the Gaussian code from the structures that we have obtained with DMHM and for these symmetrized structures we have performed wavefunction optimization. When using the DMOL code we have chosen the extended basis set since it is considered as the most reliable. When using the Gaussian code, we have tested 6-311G, 6-311G(2d) and cc-pVTZ as basis set. In Table 7.2 we present the results. As one can see, when using 6-311G(2d) and cc-pVTZ we obtain results which differ by less than 1.6

Cluster	10th	9th	8th	7th	6th	5th	4th	3rd	2nd	1st
Si_7	96.0	83.7	81.4	77.7	71.9	58.2	37.1	36.5	29.8	0.0
Si_8	30.1	28.1	22.1	21.5	19.9	16.2	15.8	15.3	15.2	0.0
Si_9	39.0	32.0	27.6	25.7	24.7	23.3	21.2	15.8	13.2	0.0
Si_{10}	54.1	39.5	36.8	30.7	29.1	27.4	21.2	18.6	6.9	0.0
Si_{11}	19.7	18.4	16.7	16.1	15.1	14.9	12.3	10.2	0.8	0.0
Si_{12}	27.8	27.8	27.5	27.4	27.3	25.5	25.0	23.9	15.6	0.0
Si_{13}	9.2	7.7	6.2	5.1	4.5	4.2	3.0	1.2	0.9	0.0
Si_{14}	15.4	14.3	12.4	11.7	8.3	6.8	5.7	2.2	2.1	0.0
Si_{15}	19.4	18.6	14.6	14.2	13.9	11.2	11.0	11.0	4.2	0.0
Si_{16}	10.5	10.1	9.6	8.9	8.5	6.3	6.2	5.6	5.2	0.0
Si_{17}	9.6	8.8	8.5	8.2	7.7	7.6	7.5	6.4	3.1	0.0
Si_{18}	18.6	17.3	16.7	16.4	16.1	9.8	9.5	9.5	8.8	0.0
Si_{19}	14.5	14.3	14.2	13.4	9.6	8.9	7.0	5.6	3.2	0.0

Table 7.1: The PBE energies in mHa for the lowest 10 configurations for Si clusters Si_n in the size range $7 \leq n \leq 19$. The PBE global minimum (1st lowest) energy was chosen as reference energy and set to 0.

mHa. In contrast, 6-311G is clearly insufficient to provide reliable results. For further calculations with Gaussian we will therefore use 6-311G(2d). When using CPMD, we have tested the parameter sets cell/cutoff 24 Å/28 Rydberg and cell/cutoff 30 Å/35 Rydberg. The discrepancies between the two parameter sets are less than 0.2 mHa as one can see in Table 7.3. In order to obtain high accuracy, we will use cell/cutoff 30 Å/35 Rydberg for further CPMD calculations.

7.4 The PBE, B3LYP and QMC results for selected clusters

Even though the PBE exchange-correlation functional is considered to be among the most accurate ones, its accuracy is clearly insufficient to determine unambiguously the energetic ordering of the configurations. For this reason R. Hennig has performed together with C. Umrigar for a number of symmetrized structures the most accurate electronic structure calculations that are feasible, namely Quantum Monte Carlo (QMC) simulations. The QMC calculations were performed using the CHAMP code developed by Umrigar and Filippi. The 1s, 2s and 2p electrons of Si were eliminated using a relativistic Hartree-Fock pseudopotential [100]. A Slater-Jastrow type wave function was used as the trial wave function. The orbitals of the Slater determinant were taken from a DFT calculation with the GAMESS [101] code using the B3LYP functional. The parameters of the Jastrow function describing electron-electron, electron-nuclear and electron-electron-nuclear correlations were optimized in variational Monte Carlo using energy minimization [102].

Cluster	Gaussian / 6-311G	Gaussian / 6-311G(2d)	Gaussian / cc-pVTZ
Si_{16a}	3.9	-3.7	-3.7
Si_{16b}	-10.2	1.4	1.2
Si_{17a}	11.3	2.7	4.1
Si_{17b}	2.5	8.4	8.5
Si_{18a}	1.7	10.2	11.8
Si_{19a}	21.6	-1.9	-1.3

Table 7.2: The energy differences in mHa without zero-point energy correction between the new low energy geometries Si_{16a}, Si_{16b}, Si_{17a}, Si_{17b}, Si_{18a} and Si_{19a} found with DMHM and the putative global minimum structures Si_{16}, Si_{17}, Si_{18} and Si_{19} using the PBE exchange-correlation functional as implemented in GAUSSIAN. The structures were first symmetrized and relaxed with B3LYP/6-311G(2d)/GAUSSIAN by R. Hennig and subsequently these symmetrized structures were taken as input structures for the wavefunction optimization with
1) PBE/GAUSSIAN, all-electron, basis set 6-311G
2) PBE/GAUSSIAN, all-electron, basis set 6-311G(2d)
3) PBE/GAUSSIAN, all-electron, basis set cc-pVTZ

Cluster	CPMD / 24Å-28 Ryd.	CPMD / 30Å-35 Ryd.
Si_{16a}	-5.9	-6.0
Si_{16b}	0.8	0.9
Si_{17a}	2.7	2.6
Si_{17b}	8.3	8.4
Si_{18a}	10.2	10.0
Si_{19a}	-4.0	-4.2

Table 7.3: The energy differences in mHa without zero-point energy correction between the new low energy geometries Si_{16a}, Si_{16b}, Si_{17a}, Si_{17b}, Si_{18a} and Si_{19a} found with DMHM and the putative global minimum structures Si_{16}, Si_{17}, Si_{18} and Si_{19} using the PBE exchange-correlation functional as implemented in CPMD, DMOL and GAUSSIAN. The structures were first symmetrized and relaxed with B3LYP/6-311G(2d)/GAUSSIAN by R. Hennig and subsequently these symmetrized structures were taken as input structures for the wavefunction optimization with
1) PBE/CPMD, relativistic Goedecker-pseudopotential, plane waves, cell/cutoff: 24 Å/28 Rydberg.
2) PBE/CPMD, relativistic Goedecker-pseudopotential, plane waves, cell/cutoff: 30 Å/35 Rydberg.

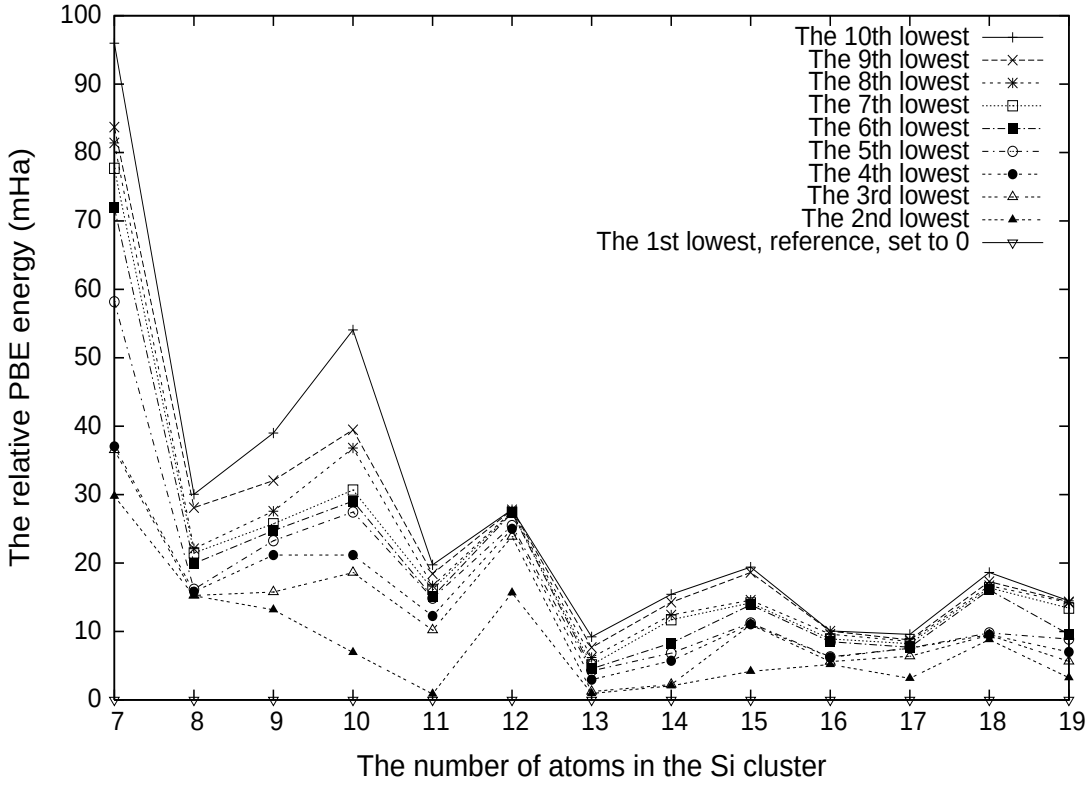

Figure 7.2: The dependence of the PBE energy interval for the lowest 10 configurations on the cluster size.

Diffusion Monte Carlo method calculated the final energies, which are presented in Table I. The corresponding configurations are shown in Fig. 7.3. Monte Carlo simulations have error bars of the order of 1mHa which is just enough to discriminate the different energies. Even though the Monte Carlo results change the energetic ordering of the PBE results, the central feature remains. Different configurations have energies that are nearly identical. Table 7.4 also shows that the various high quality basis sets used by different electronic structure programs give slightly different answers that might change the energetic ordering. The new low-lying structures Si_{16a}, Si_{16b}, Si_{17a}, Si_{17b}, Si_{18a} and Si_{19a} which were found with DMHM and the reference structures Si_{16} [5], Si_{17} [8], Si_{18} [8] and Si_{19} [9] were already presented in [99]. The structure Si_{13} was found by Ho [8], the rotationally symmetric Si_{13d} structure was recently proposed by B.Hartke [4], Si_{13f} by Röthlisberger [103] and Si_{13g} by J.Jeong et al. [104]. Using DMHM [99] we have found new low-lying structures Si_{13a}, Si_{13b}, Si_{13c} and Si_{13e}. Apparently, from the QMC results in Table 7.4 we can conclude that the Si_{13d} and Si_{13a} configurations can be considered as the lowest energy structures. The new Si_{13a} structure found with DMHM contains the stable Si_6 subunit [105]. From Table 7.4 and Fig.D.13 one can also see when comparing the QMC results for Si_{16}/Si_{16a}, Si_{19}/Si_{19a} and Si_{13a}/Si_{13} that the structures Si_{16}, Si_{19} and

Cluster	B3LYP/ GAUS.	PBE/ DMOL	PBE/ CPMD	PBE/ GAUS.	DMC
Si_{13}	0.0	0.0	0.0	0.0	0.0
Si_{13a}	-11.7	6.3	7.1	5.3	-3.3±1.0
Si_{13b}	-1.4	9.5	13.2	11.5	5.7±1.0
Si_{13c}	8.6	4.7	3.1	3.1	6.4±1.0
Si_{13d}	-6.7	-2.9	0.9	0.6	-5.7±1.1
Si_{13e}	3.6	3.9	4.1	4.2	6.1±1.0
Si_{13f}	4.2	7.0	8.5	8.0	10.6±1.0
Si_{13g}	-6.3	-0.8	2.6	2.3	0.0±1.1
Si_{16}	0.0	0.0	0.0	0.0	0.0
Si_{16a}	24.0	-0.2	-6.0	-3.7	9.9±1.4
Si_{16b}	9.5	0.9	0.9	1.4	8.3±1.4
Si_{17}	0.0	0.0	0.0	0.0	0.0
Si_{17a}	7.4	8.4	2.6	2.7	6.3±1.5
Si_{17b}	10.2	11.6	8.4	8.4	13.2±1.7
Si_{18}	0.0	0.0	0.0	0.0	0.0
Si_{18a}	31.3	17.1	10.0	10.2	23.9±1.6
Si_{19}	0.0	0.0	0.0	0.0	0.0
Si_{19a}	15.4	-1.0	-4.2	-1.9	2.1 ±1.7

Table 7.4: The energy differences in mHa between the low energy geometries Si_{13a}, Si_{13b}, Si_{13c}, Si_{13d}, Si_{13e}, Si_{13f}, Si_{16a}, Si_{16b}, Si_{17a}, Si_{17b}, Si_{18a}, Si_{19a} and the reference structures Si_{13}, Si_{16}, Si_{17}, Si_{18} and Si_{19}, that were proposed in earlier publications as density functional global minimum structures. For the Gaussian [106] calculations the 6-311G(2d) basis set was used and for the DMol3 version 2005 [87], [88] calculations the extended basis set. The CPMD [89] calculations used an accurate pseudopotential [92] with a 35 Rydberg plane wave cutoff and a 30 Å simulation cell.

Si_{13a} containing a Si_6 subunit are energetically favored within QMC over structures Si_{16a}, Si_{19a} and Si_{13} that contain a tricapped trigonal prism (TTP) subunit.

7.5 Temperature effects on the energy order

7.5.1 Overview

After having discussed the limitations of computational approaches in determining the total energy of silicon clusters with the necessary accuracy let us discuss the physical effects that can change the energetic ordering. For the Si_{13}, Si_{13a} and Si_{13d} clusters we have zero point energies of 24.0, 25.0 and 24.5 mHa. For the Si_{19} and Si_{19a} we have zero point energies of 38.8 and 38.0 mHa. So the differences of the zero point energies are all of the order of mHa and are thus not negligible, but do not change the energetic ordering for

the clusters we studied. In order to study the entropy effects we calculated the rotational and vibrational free energies based on the harmonic frequencies obtained from density functional (PBE) calculations [107].
The total free energy can be written as

$$E_f = E_e - k_B T \ln q_{tot} = E_e - k_B T \ln[q_{trans} q_{vib} q_{rot}] \quad , \tag{7.1}$$

where q_{trans}, q_{vib} and q_{rot} are the translational, the vibrational and the rotational partition functions respectively. The translational partition function depends only on the mass M of the molecule and does not depend on its geometry. For this reason it was not considered. The total free energy can thus be written as

$$E_f = E_e - k_B T \ln[q_{vib} q_{rot}] = E_e + E_{vib} + E_{rot} \tag{7.2}$$

with

E_e being the electronic total energy obtained from DFT or QMC,
$E_{vib} = -k_B T \ln q_{vib}$ being the vibrational free energy and
$E_{rot} = -k_B T \ln q_{rot}$ being the rotational free energy.

The partition function is defined as a sum of exponential terms involving all possible quantum energy states:

$$q = \sum_{i}^{\text{all states}} e^{-\frac{\epsilon_i}{k_B T}} \tag{7.3}$$

7.5.2 Molecular vibrations

Molecular vibrations can be described in the lowest approximation by a harmonic oscillator. The energy of a diatomic molecule with an internuclear distance R is given by

$$E(R) \approx E_0 + \frac{1}{2}\frac{d^2E}{dR^2}(R - R_0)^2 = \frac{1}{2}k(R - R_0)^2 \tag{7.4}$$

with R_0 being the equilibrium distance. The energy levels obtained from the Schrödinger equation for a one-dimensional harmonic oscillator representing a system of two atoms are given by

$$\epsilon_{vib} = (n + \frac{1}{2})h\nu \tag{7.5}$$

with

$$\nu = \frac{1}{2\pi}\sqrt{\frac{k}{\mu}} \quad , \tag{7.6}$$

where μ is the reduced mass, ν the vibrational frequency and n a quantum number with $0 \leq n < \infty$. The vibrational partition function for a diatomic system can be written according to the Eq.7.3 as

$$q_{vib} = \sum_{n=0}^{\infty} e^{-(n+\frac{1}{2})\frac{h\nu}{k_B T}} = e^{-\frac{h\nu}{2k_B T}} \sum_{n=0}^{\infty} e^{-\frac{nh\nu}{k_B T}} = \frac{e^{-\frac{h\nu}{2k_B T}}}{1 - e^{-\frac{h\nu}{k_B T}}}. \tag{7.7}$$

For a polyatomic molecule the force constant k is replaced by the Hessian matrix, which is a $3N \times 3N$ matrix with the second derivatives of the energy with respect to the atomic coordinates as entries. By a transformation to a new coordinate system called vibrational normal modes this matrix can be brought to a diagonal form. Of 3N degrees of freedom 3 describe pure translations, another 3 describe rotations and 3N-6 are left for vibrations. Taking into account Eq.7.7 the vibrational partition function for a polyatomic system can be written as

$$q_{vib} = \prod_{i=1}^{3N-6} \frac{e^{-\frac{h\nu_i}{2k_B T}}}{1 - e^{-\frac{h\nu_i}{k_B T}}} \quad . \tag{7.8}$$

7.5.3 Molecular rotations

As for rotations, it can be assumed in the lowest approximation that the centrifugal forces which are experienced by the nuclei of a rotating molecule are small, and that rotations do not alter the geometry of the molecule. Centrifugal corrections and vibrational-rotational couplings are usually of the order of a few % and can be neglected up to temperatures of $\sim$1000 K. The spacing between the rotational energy levels is much smaller than $k_B T$ at room temperatures so that the sum in Eq.7.3 can be replaced by an integral. One obtains for the rotational partition function the expression

$$q_{rot} = \frac{\sqrt{\pi}}{\sigma}\left(\frac{8\pi^2 k_B T}{h^2}\right)^{3/2}\sqrt{I_1 I_2 I_3}. \tag{7.9}$$

The symmetry index σ is the order of the rotational subgroup in the molecular point group (for example it is 2 for H_2O and it is 3 for NH_3). I_1, I_2, I_3 are the moments of inertia, i.e. the eigenvalues of the moment of inertia tensor. They can be calculated using the principal axes transformation, which is described in detail in Appendix 2.

7.5.4 Impact of entropy effects on Si clusters

We have first calculated the sum of the rotational and vibrational free energies $E_{vib} + E_{rot}$ using equations 7.8 and 7.9 for a number of configurations. If one compares the sum of the rotational and vibrational free energies $E_{vib} + E_{rot}$ for non-symmetric configurations, one typically finds differences of about 0.5 mHa at room temperature and about 1 mHa close to the melting point of the clusters [108]. This might change the energetic ordering, but we did not find a case where it actually does. When comparing non-symmetric configurations the difference in $E_{vib} + E_{rot}$ can be neglected in most cases. The situation is different if one compares a symmetric with a non-symmetric configuration.
Silicon occurs in nature mainly as ^{28}Si or ^{29}Si isotope. The predominant isotope for silicon ^{28}Si (abundance $\sim$92 % [1]) has mass 28 and no nuclear spin, the ^{29}Si isotope (abundance $\sim$5 % [1]) has mass 29 and nuclear spin 1/2. When studying configurations with rotational symmetry, we will consider pure clusters consisting only of ^{28}Si atoms since the presence of a ^{29}Si atom would destroy the rotational symmetry. One can easily estimate from the abundances of the isotopes that $\sim$34 % of Si_{13} clusters will be pure clusters. Such clusters could be also produced from pure ^{28}Si probe. For a pure cluster with rotational symmetry, the order of the rotational subgroup enters into the formula for the rotational free energy. This leads to a weaker decrease of the free energy for symmetric configurations compared to non-symmetric configurations and favors thus non-symmetric structures. In Fig. 7.4 we present the free energy curves for the structures Si_{13a} and Si_{13d} as a function of temperature with the Si_{13} free energy chosen as reference energy. The band structure for Si_{13a} and Si_{13d} is due to the statistical errors in QMC with respect to the structure Si_{13}. For the symmetric Si_{13a} configuration the order of the rotational subgroup is 3, for Si_{13d} it is 2 and for Si_{13} it is 1. This leads to a reversal of the energetic ordering of the structures Si_{13} and Si_{13a} in the interval between 250 and 650 K as shown in the Fig. 7.4. Because of the entropy effect the Si_{13} configuration which is the highest at zero temperature even becomes the lowest at temperatures above 1000 K. At room temperature the Si_{13a} and Si_{13d} bands are separated by an energy gap in the range between $\sim$1.2mHa and $\sim$5.5mHa. This corresponds to a Boltzmann weight in the range between 0.7% and 30%. These considerations are valid if one considers clusters consisting only of ^{28}Si atoms. Things change if one takes into account the presence of a ^{29}Si isotope which destroys the rotational symmetry and makes the considerations above inapplicable. One can estimate from the abundances of the isotopes that $\sim$24 % of Si_{13} clusters will contain one ^{29}Si isotope. If one ^{28}Si atom with nuclear spin 0 is replaced by a ^{29}Si isotope which has spin 1/2, the nuclear wave-function is a doublet and additional degeneracy comes from

the fact that the isotope can replace any of the atoms. For a non-symmetric cluster with N atoms the degeneracy is thus $2N$. For a symmetric cluster that has several equivalent atoms the degeneracy is however reduced. In the case of the Si_{13a} structure there are for instance only 5 non-equivalent sites, Si_{13d} has 6 and Si_{13} has 9. The nuclear entropy thus favors Si_{13} over Si_{13d} by $-kT\ln(\frac{9}{6})$ which is ~ 0.4 mHa at room temperature. In addition, the vibrational and rotational entropy contributions are slightly changed by the presence of an isotope leading to an effect of the same order of magnitude.

7.6 Configurational density of states

Up to now we have concentrated on the 10 lowest structures. Considering higher lying configurations, the energetic spacing between configurations decreases even further. This can be inferred from the fact the the configurational density of states, defined as the number of configurations per energy interval, increases strongly. Fig.7.5 illustrates this behavior for the Si_{17} cluster. The density of states was calculated on the basis of the results obtained with DMHM using the QUICKSTEP code and LDA exchange-correlation functional. We have explored regions with up to 100 mHa above the global minimum. However, we have chosen a cutoff of 35 mHa above the global minimum in Fig.7.5, since due to the drastic increase of the configurational density higher energy regions could not be explored thoroughly enough. What makes the DMHM effective when searching for the global minimum is the thorough exploration of the energy regions slightly above the global minimum.

7.7 Coexistence of clusters with different coordination numbers

On the basis of the Fig.7.1 we have calculated coordination numbers of various low-lying Si_{17} configurations. We have chosen a soft cutoff between 3.0 and 3.2 Angstroem (5.7 and 6.0 a.u.) for the first nearest neighbor, i.e. only Si atoms with a distance smaller than 3.2 Angstroem (6.0 a.u.) are considered as first nearest neighbors. The results are presented in Fig.7.6. Apparently, the preference for high-coordination numbers for low energy configurations is rather weak.

7.8 Summary

We have shown that there exists a large number of configurations for certain silicon clusters that are energetically extremely close to the ground state. This feature was observed for Si_{13} and Si_{19} and it will presumably be even more important for larger cluster sizes that were not studied in this work. As a consequence, entropy effects that are usually neglected can change the energetic ordering of the lowest configurations. Entropy is in particular disfavoring symmetric clusters Si_n in the range $13 \leq n \leq 19$ which contain in most cases no ^{29}Si isotope or one ^{29}Si isotope. Larger clusters will on average contain more than one ^{29}Si isotope and the symmetry related effects discussed above do not exist. However, for larger clusters the 10 lowest configurations can be expected to lie within a tinier interval. Entropy effects not related to symmetry considerations might thus easily change the energy order of clusters with more than 19 atoms. Even if there is no reordering, different structures can be so close in free energy that a mixture of two or more configurations will be found at thermal equilibrium. As a consequence measured properties of clusters can be some average of the properties of several low-lying isomers.

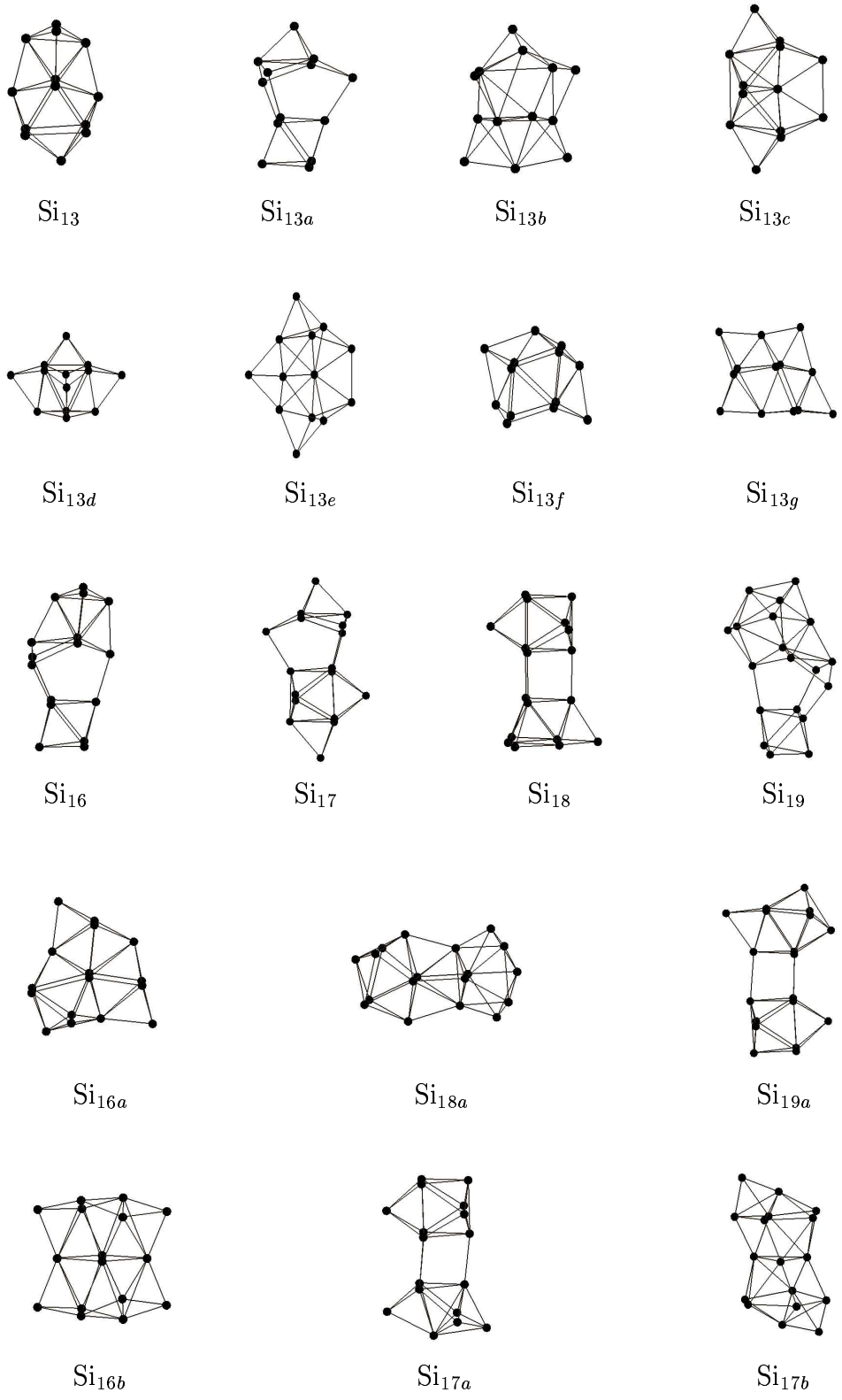

Figure 7.3: Symmetrized geometries of low-lying Si_{13}, Si_{16}, Si_{17}, Si_{18} and Si_{19} isomers.

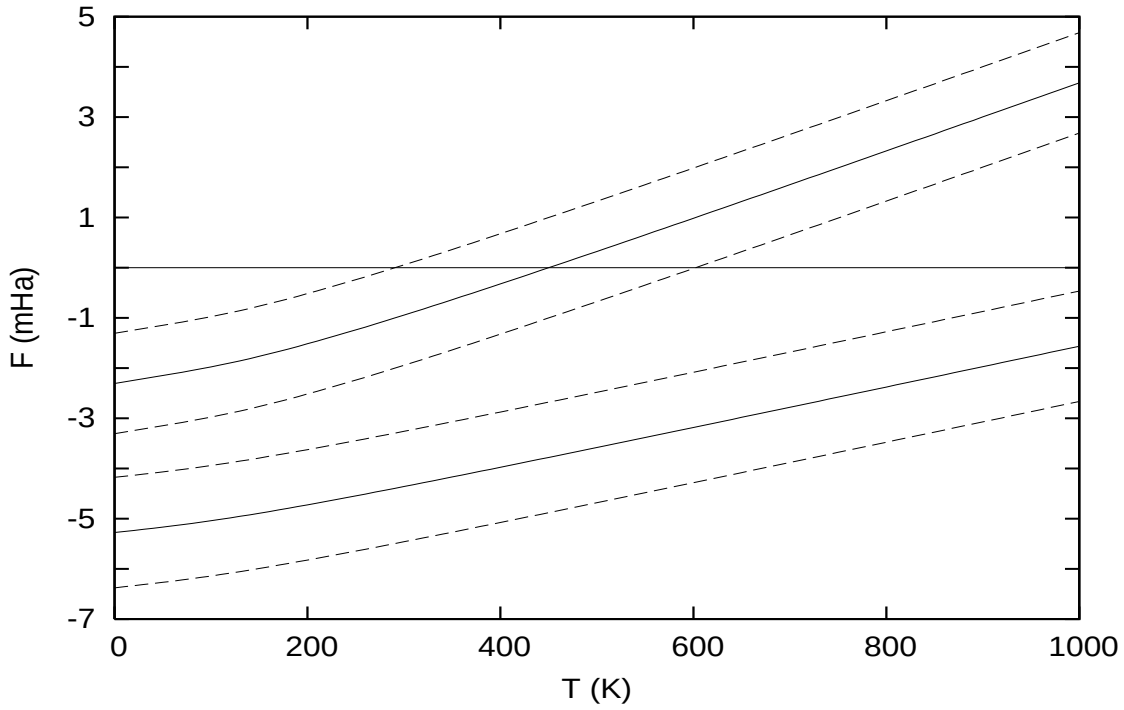

Figure 7.4: The sum of the electronic (QMC, with errors), vibrational (including zero point) and rotational free energy contributions for Si_{13a} (upper band) and Si_{13d} (lower band) configurations as a function of temperature with the Si_{13} (set to 0, solid line) free energy chosen as reference energy.

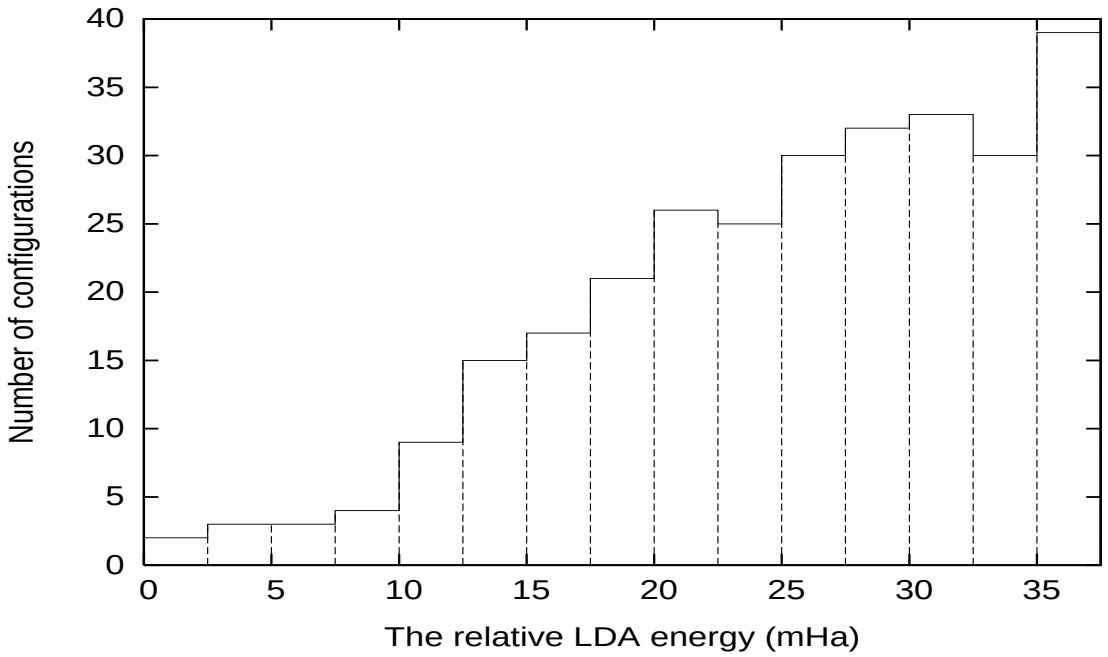

Figure 7.5: The configurational density of states for Si_{17}.

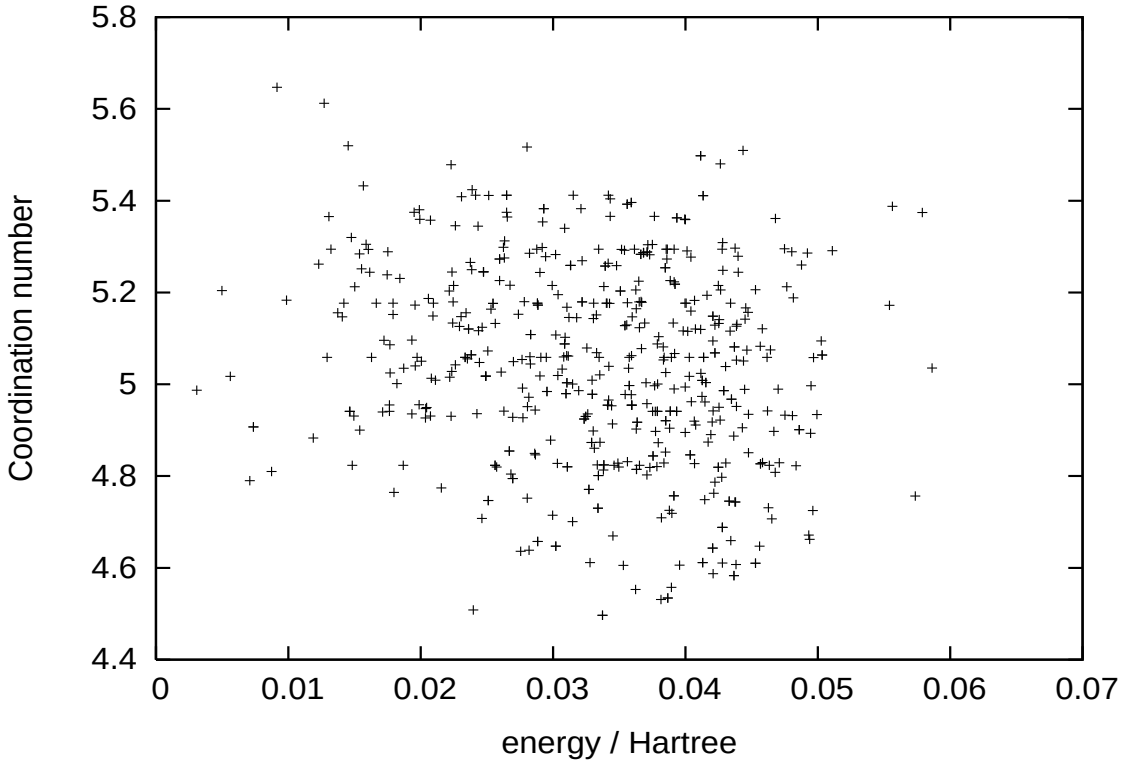

Figure 7.6: The coordination number of various low-lying Si_{17} configurations in dependence on energy.

Chapter 8

Conclusion

The DMHM has been proved to be a powerful global optimization algorithm which can rapidly find the global minimum of complex systems within DFT provided that there exists a fast method that can evaluate the potential energy surface less accurately. The memory feedback prevents the algorithm from being trapped in a wrong funnel which does not contain the global minimum and favors search in new unexploited regions of the configurational space. The possibility of adjustment of the parameters β_1, β_2 and β_3 as well as of the parameters α_1 and α_2 makes the DMHM very flexible and can tailor it to the needs of the specific physical problem. In particular, by setting β_1 very close to 1, the DMHM can effectively take into account the MDBEP principle if there is a good correlation between the barrier heights of the maxima along the MD trajectory using the fast method and those of true transition states. The choice of a large value for *mdmin* allows to exploit regions of the configurational space that are far from the current local minimum. Having applied the DMHM to silicon clusters Si_n in the range $7 \leq n \leq 19$ we have found virtually all global minima candidates that were reported previously in the literature and have discovered new low energy isomers for Si_{13}, Si_{16}, Si_{17}, Si_{18} and Si_{19}.
We have found that the 10 lowest configurations for silicon clusters Si_n in the range $13 \leq n \leq 19$ coexist within a tiny energy interval. Besides, the number of possible isomers as well as the configurational density of states is much higher for this size range than previously estimated, motivating to set the notion of medium-sized silicon cluster already at 13 atoms. The present DFT exchange-correlation functionals and DFT programs are not capable of reliably predicting which of the global minimum candidates is the energetically lowest since even with high-quality basis sets different DFT programs deliver different results within the same exchange-correlation functional. Only QMC calculations can provide reliable statements about the energy ordering of low energy isomers.
The rotational symmetry and the presence of isotopes play a major role in establishing the energy order for low energy silicon cluster isomers in the range $13 \leq n \leq 19$ due to the entropy effects. Pure isotope-free configurations with rotational symmetry and symmetric configurations containing one isotope ^{29}Si are disfavored by the entropy effects. From these

observations we have concluded that for silicon clusters Si_n in the range $13 \leq n \leq 19$ a mixture of several isomers according to the Boltzmann distribution is to be expected. The notion of a well defined ground state hardly makes sense in this context and interpretation of any experimental data should therefore be handled with care.
For silicon clusters containing more than 19 atoms the symmetry considerations are not applicable since isotope-free clusters are not likely to occur in this size range and many clusters will contain more than one isotope. However, the major result of our studies that the 10 lowest lying isomers coexist within a tiny energy interval can be extended to larger clusters. Experimentally, the presence of several peaks starting with Si_{17}^+ in the drift time distributions of silicon cluster cations Si_n^+ obtained in high-resolution ion mobility measurements by Hudgins et al. [3] confirms the coexistence of several isomers for medium-sized silicon clusters at room temperature. Elucidation of entropy effects remains an interesting task for researchers who are involved in the study of medium-sized silicon clusters. In particular, entropy effects will have influence on the size range of the experimentally observed non-spherical to spherical transition of medium-sized silicon clusters with more than 19 atoms.

Appendix A

The Metropolis algorithm

The Metropolis algorithm is the standard method to generate random points with a certain distribution in high dimensional spaces. Since the high dimensional random points correspond generally in physics to the configuration of some system we will use the word configuration rather than random point and we will denote such a configuration by X. The vast majority of the total configurational space of a many particle system corresponds to unphysical configurations where for instance two atoms are very close to each other. Because of the nucleus-nucleus repulsive potential this results in extremely high energies which contribute virtually nothing to a Boltzmann distribution at room temperature. Importance sampling, id est creating distributions that sample only the low energy part of the configurational space is therefore essential. The Metropolis algorithm is based on a Markov chain. In a Markov chain the next configuration X' is obtained from the present configuration X by a certain move that is characterized by a transition probability $T(X' \leftarrow X)$. The probability $P_N(X_1, X_2, ..., X_N)$ of finding a certain sequence of configurations is therefore given by

$$P_N(X_1, X_2, ..., X_N) = T(X_N \leftarrow X_{N-1})...T(X_3 \leftarrow X_2)T(X_2 \leftarrow X_1)P_1(X_1) \ , \qquad (A.1)$$

where the transition probabilities are normalized

$$\sum_{X'} T(X' \leftarrow X) = 1 \qquad (A.2)$$

and where $P_1(X)$ is an arbitrary probability distribution. In contrast, for a truly random sequence this probability would be given by

$$P_N(X_1, X_2, ..., X_N) = P_1(X_1)P_1(X_2)...P_1(X_N) \ . \tag{A.3}$$

For Markov processes it is convenient to introduce the notion of a walker. Instead of saying that one configuration is obtained form another we will say that the walker goes from one configuration to another. The notion of a walker gives a more intuitive description of a Markov process. The simplest example of a Markov process is a random walk on a 2-dimensional square lattice. Each node represents a configuration. At any step the walker can jump to any of its 4 nearest neighbors, id est $T(X' \leftarrow X) = \frac{1}{4}$. Let us now introduce the function $P(X,t)$ which gives the probability of finding a walker at configuration X at Markovian step t. The probability $P(X, t+1)$ is then given by

$$P(X,t) + \sum_{X'} T(X \leftarrow X')P(X',t) - \sum_{X'} T(X' \leftarrow X)P(X,t) \ . \tag{A.4}$$

At equilibrium P(X,t+1)=P(X,t)=P(X) and hence

$$\sum_{X'} T(X \leftarrow X')P(X',t) = \sum_{X'} T(X' \leftarrow X)P(X,t) \ . \tag{A.5}$$

This equation is satisfied under the condition of detailed balance:

$$T(X \leftarrow X')P(X',t) = T(X' \leftarrow X)P(X,t) \ . \tag{A.6}$$

Ensemble averages can be assumed to be equal to time averages for an ergodic system. Observing the movement of one walker, we can numerically calculate time averages. Since the distribution of walkers P(X,t) tends to P(X) provided that the detailed balance conditions are satisfied, we can write

$$P(X) = \lim_{T \to \infty} \frac{1}{T} \sum_{t=1}^{T} P(X,t) \ . \tag{A.7}$$

The transition probability in a Markov process consists of two parts, a trial step probability $\omega_{X,X'}$ and an acceptance probability $A_{X,X'}$:

$$T(X' \leftarrow X) = \omega_{X',X} A_{X',X}. \tag{A.8}$$

The trial step probability $\omega_{X,X'}$ has to be symmetric, id est $\omega_{X',X} = \omega_{X,X'}$, and so the detailed balance condition in Eq. $A.6$ gives:

$$\frac{A_{X,X'}}{A_{X',X}} = \frac{P(X)}{P(X')}. \tag{A.9}$$

The Metropolis acceptance prescription accepts a trial step if the probability of the new configuration X' is larger than that of the old configuration X and accepts it with a probability $\frac{P(X')}{P(X)}$ in the opposite case:

$$A_{X',X} = \begin{cases} 1 & \text{if} \quad P(X') > P(X) \\ \frac{P(X')}{P(X)} & \text{if} \quad P(X') < P(X) \end{cases}$$

This choice obviously satisfies Eq. $A.9$. Accepting with a certain probability is done in the following way numerically. A random number, equally distributed in the interval [0:1] is generated by calling a random number generator. If this random number is less than $\frac{P(X')}{P(X)}$ the step is accepted, otherwise it is rejected. The trial step probabilities do not enter into the Metropolis acceptance criterion in Eq. $A.10$. Nevertheless they play an important role. First, they have obviously to be chosen in such a way that any configuration of the system can be reached. Second, their choice determines how fast the equilibrium distribution P(X) is reached. With a bad choice, it may well turn out that the equilibrium distribution can not be reached within the available computer time.

Appendix B

The principal axes transformation

The inertia tensor for a molecule consisting of N atoms with masses m_i and coordinates x_i, y_i, z_i is given by a symmetric matrix:

$$I = \begin{pmatrix} \sum_{i=1}^{N} m_i(y_i^2 + z_i^2) & -\sum_{i=1}^{N} m_i x_i y_i & -\sum_{i=1}^{N} m_i x_i z_i \\ -\sum_{i=1}^{N} m_i x_i y_i & \sum_{i=1}^{N} m_i(x_i^2 + z_i^2) & -\sum_{i=1}^{N} m_i y_i z_i \\ -\sum_{i=1}^{N} m_i x_i z_i & -\sum_{i=1}^{N} m_i y_i z_i & \sum_{i=1}^{N} m_i(x_i^2 + y_i^2) \end{pmatrix}. \tag{B.1}$$

By choosing a suitable coordinate transformation α this symmetric matrix can be diagonalized:

$$I_D = \alpha I \alpha^T = \begin{pmatrix} p_1 & 0 & 0 \\ 0 & p_2 & 0 \\ 0 & 0 & p_3 \end{pmatrix}. \tag{B.2}$$

The coordinates $\vec{r}_i = (x_i, y_i, z_i)$ are transformed according to:

$$\vec{r}_i \rightarrow \alpha^T \vec{r}_i. \tag{B.3}$$

The eigenvalues $p_1 \leq p_2 \leq p_3$ are called the principal moments of inertia and the eigenvectors are called the principal axes of inertia. One can distinguish 3 cases depending on the shape of the structure:

1) $p_1 \approx p_2 < p_3$: oblate structure (example: pancake);
2) $p_1 \approx p_2 \approx p_3$: spherical (example: sphere);
3) $p_1 < p_2 \approx p_3$: prolate structure (example: cylinder).

One can also subdivide the structures in two classes:

1) $p_3/p_1 \approx 1$: spherical;
2) $p_3/p_1 > 1$: non-spherical.

Transforming the coordinates of a cluster into the principal axes system and calculating the principal moments of inertia p_1, p_2 and p_3 allows thus to characterize the shape of the cluster by a set of numbers. The principal axes transformation is also important if one wants to compare the DFT energies of different clusters that were obtained by a periodic systems DFT code, since varying the orientation of the cluster within the box may slightly change its DFT energy due to the interaction with the periodic images. Besides, transforming the cluster into the principal axes system enables its effective visualization and makes it easier to compare its geometry to other geometries when dealing with an ensemble of clusters.

Appendix C

Rotational and vibrational temperatures of Si_{13}, Si_{13a} and Si_{13d}

The rotational and vibrational temperatures are commonly used to simplify the calculation of the partition functions. The rotational temperatures are calculated according to

$$\Theta_r = \frac{h^2}{8\pi^2 p_i k_B} \tag{C.1}$$

with p_i $(1 \leq i \leq 3)$ being the principal moments of inertia. The vibrational temperatures are calculated according to

$$\Theta_r = h\nu/k_B \quad . \tag{C.2}$$

We present the calculated results for Si_{13}, Si_{13a} and Si_{13d} below.

Rotational temperatures in K:

Si_{13}	0.020	0.014	0.012
Si_{13a}	0.020	0.012	0.012
Si_{13d}	0.018	0.015	0.012

Vibrational temperatures (purified) in K:

Si_{13}:

234.052	275.396	278.859
288.750	288.883	310.071
340.066	341.547	360.880
361.851	379.097	382.395
390.429	408.954	414.670
425.119	449.236	453.587
478.994	491.597	497.030
502.537	513.568	534.672
554.668	581.785	589.697
619.387	647.464	652.310
700.003	714.263	724.775

$\underline{\text{Si}_{13a}}$:

263.121	264.063	275.391
278.052	312.865	324.419
328.344	332.023	373.195
379.834	383.317	385.512
391.311	400.663	414.628
423.778	427.320	494.934
518.116	526.224	558.734
568.761	582.542	598.035
609.573	622.777	623.866
633.069	640.045	676.496
710.621	724.804	767.046

$\underline{\text{Si}_{13d}}$:

260.204	281.897	312.719
319.389	321.980	329.264
330.057	341.734	351.407
358.040	359.881	371.279
381.273	393.182	395.024
405.720	438.088	456.022
460.795	500.877	517.593
528.956	570.802	584.240
599.120	606.919	609.757
611.310	649.076	686.988
703.520	703.965	712.834

Appendix D

The geometries of the 10 lowest energy clusters in the size range from Si_7 to Si_{19}

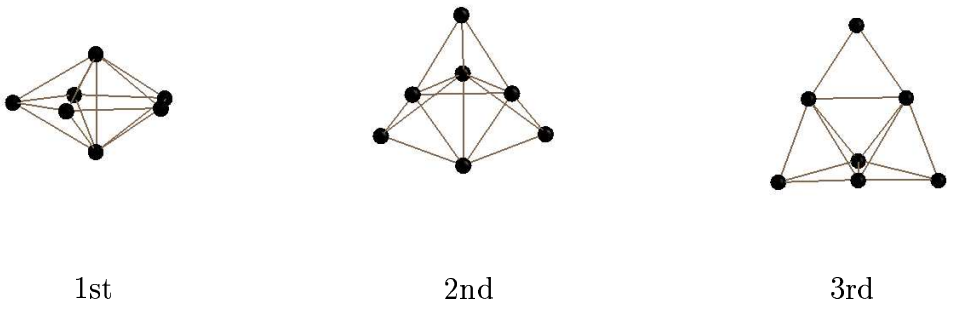

1st 2nd 3rd

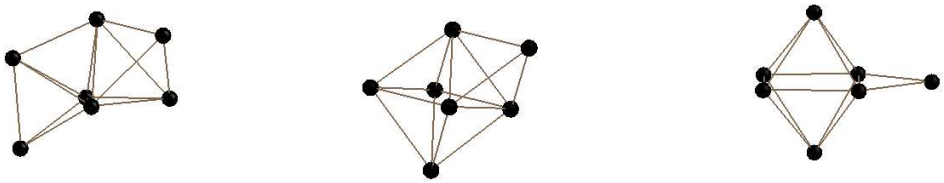

4th 5th 6th

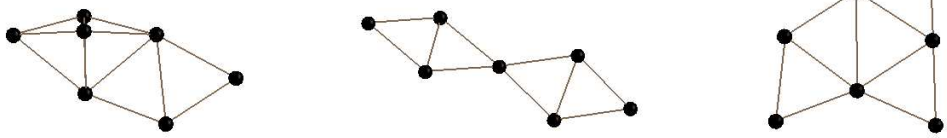

7th 8th 9th

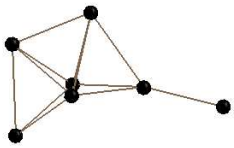

10th

Figure D.1: Geometries of the 10 lowest Si_7 isomers.

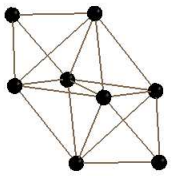

1st

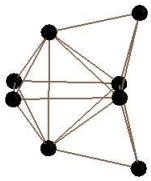

2nd

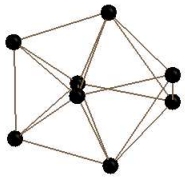

3rd

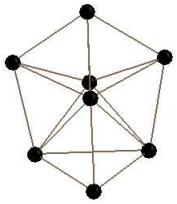

4th

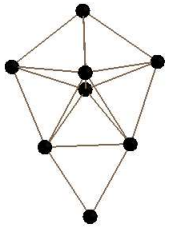

5th

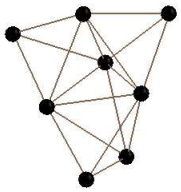

6th

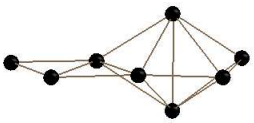

7th

8th

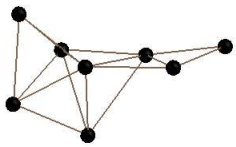

9th

10th

Figure D.2: Geometries of the 10 lowest Si_8 isomers.

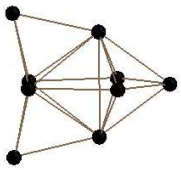

1st

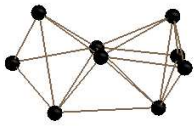

2nd

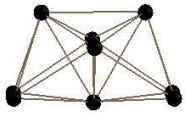

3rd

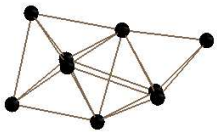

4th

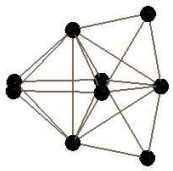

5th

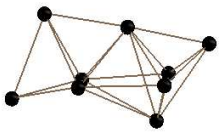

6th

7th

8th

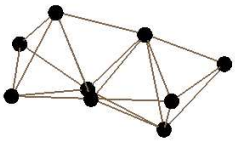

9th

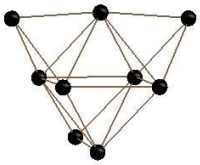

10th

Figure D.3: Geometries of the 10 lowest Si_9 isomers.

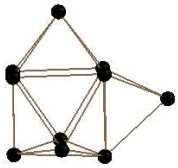

1st

2nd

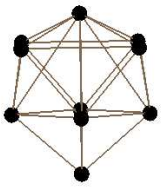

3rd

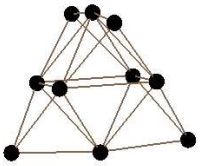

4th

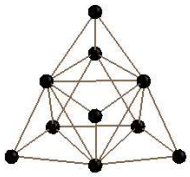

5th

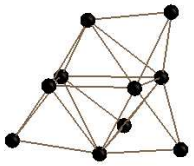

6th

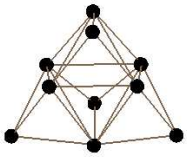

7th

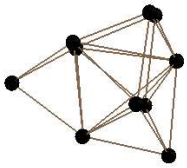

8th

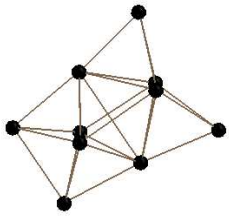

9th

10th

Figure D.4: Geometries of the 10 lowest Si_{10} isomers.

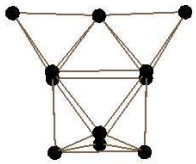

1st

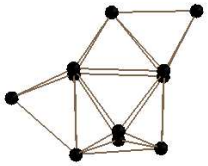

2nd

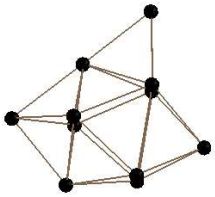

3rd

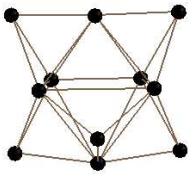

4th

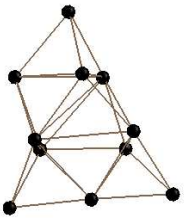

5th

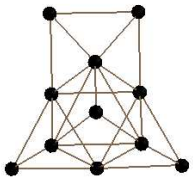

6th

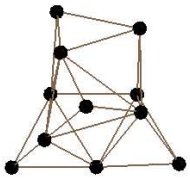

7th

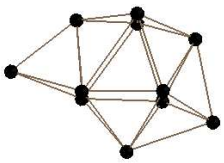

8th

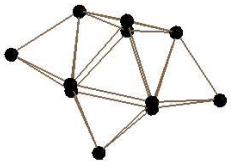

9th

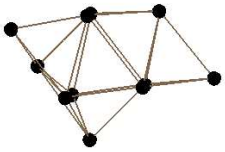

10th

Figure D.5: Geometries of the 10 lowest Si_{11} isomers.

1st

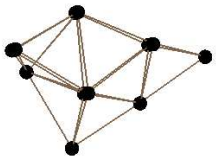

2nd

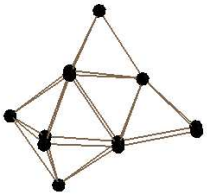

3rd

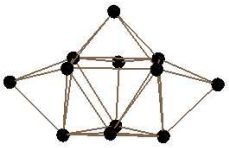

4th

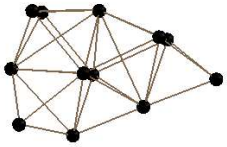

5th

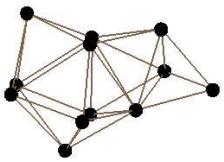

6th

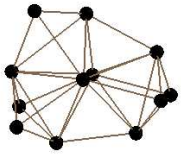

7th

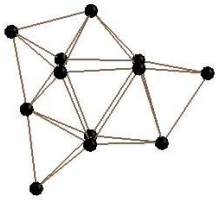

8th

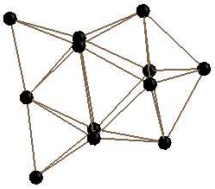

9th

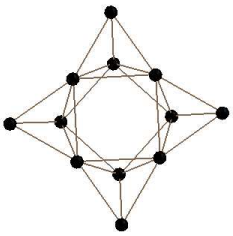

10th

Figure D.6: Geometries of the 10 lowest Si_{12} isomers.

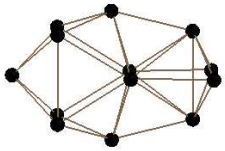

1st

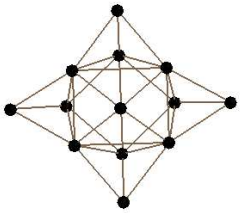

2nd

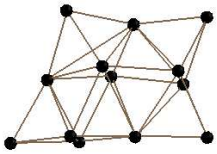

3rd

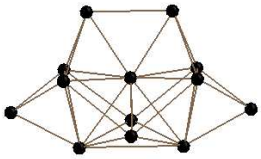

4th

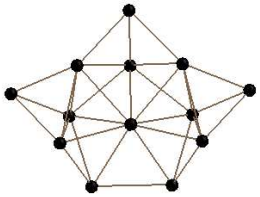

5th

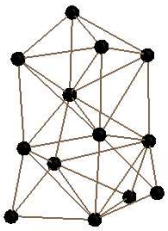

6th

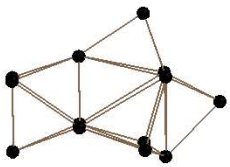

7th

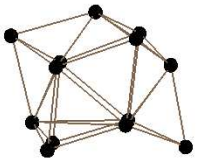

8th

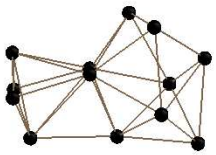

9th

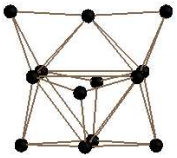

10th

Figure D.7: Geometries of the 10 lowest Si_{13} isomers.

1st

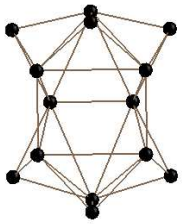

2nd

3rd

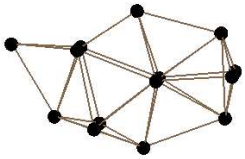

4th

5th

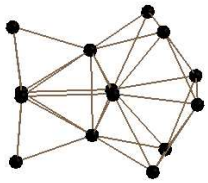

6th

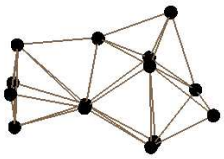

7th

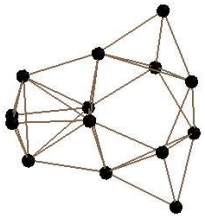

8th

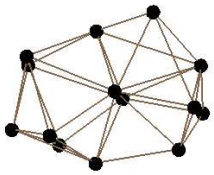

9th

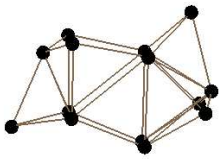

10th

Figure D.8: Geometries of the 10 lowest Si_{14} isomers.

1st

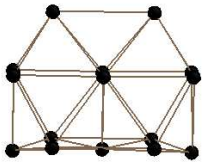

2nd

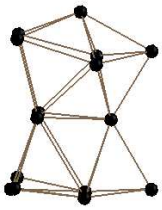

3rd

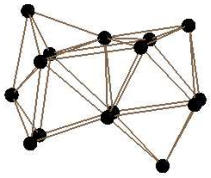

4th

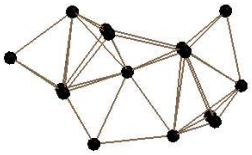

5th

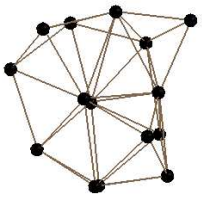

6th

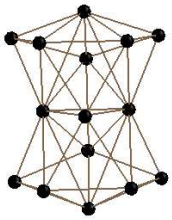

7th

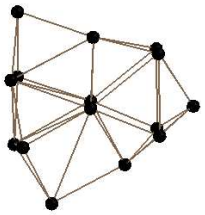

8th

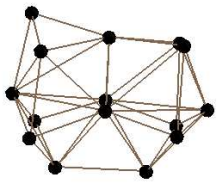

9th

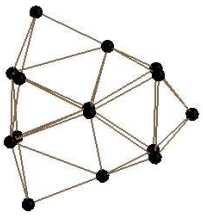

10th

Figure D.9: Geometries of the 10 lowest Si_{15} isomers.

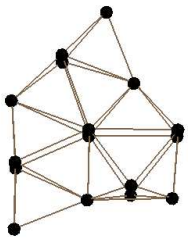

1st

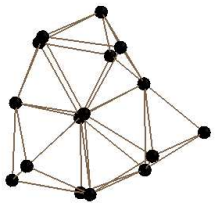

2nd

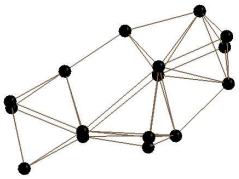

3rd

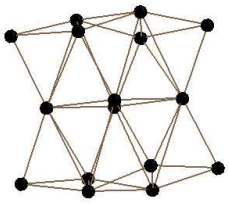

4th

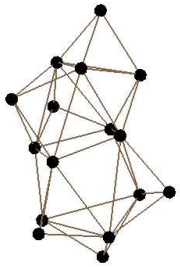

5th

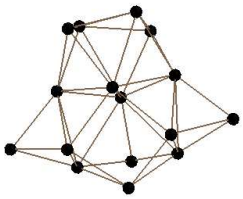

6th

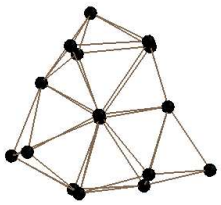

7th

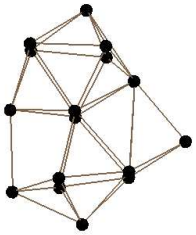

8th

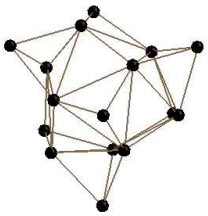

9th

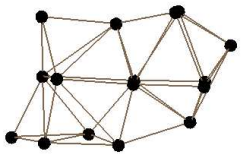

10th

Figure D.10: Geometries of the 10 lowest Si_{16} isomers.

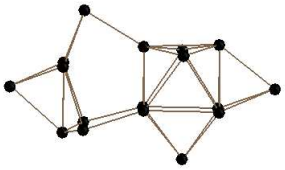

1st

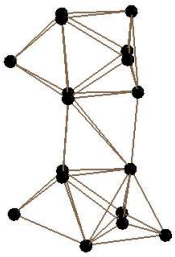

2nd

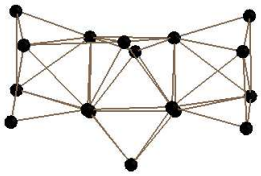

3rd

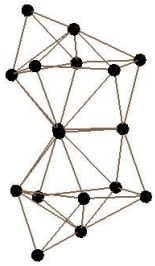

4th

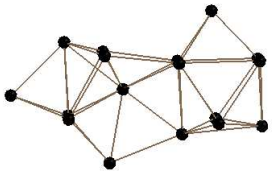

5th

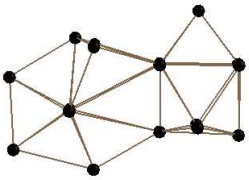

6th

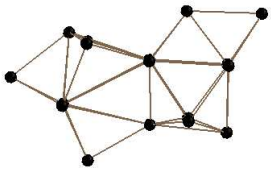

7th

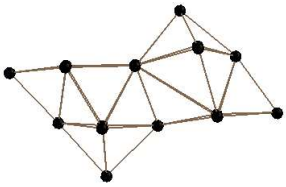

8th

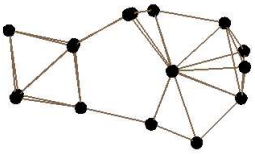

9th

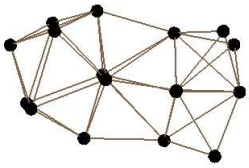

10th

Figure D.11: Geometries of the 10 lowest Si_{17} isomers.

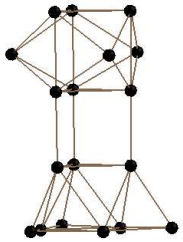

1st

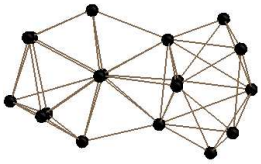

2nd

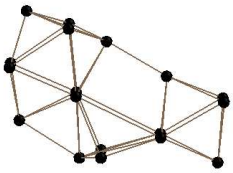

3rd

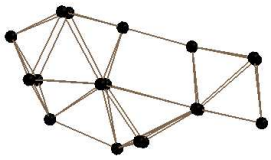

4th

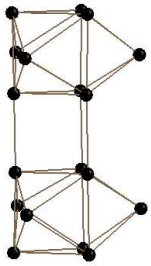

5th

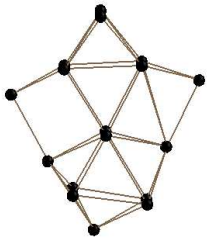

6th

7th

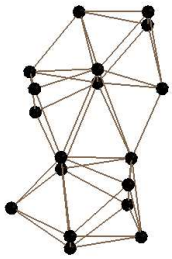

8th

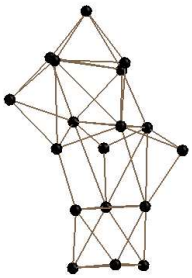

9th

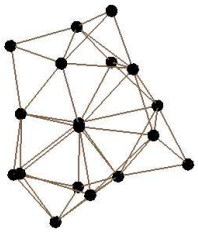

10th

Figure D.12: Geometries of the 10 lowest Si_{18} isomers.

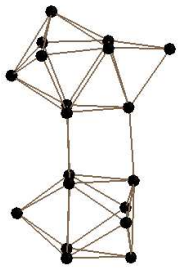

1st

2nd

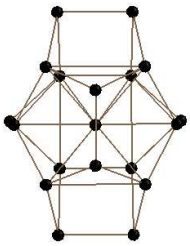

3rd

4th

5th

6th

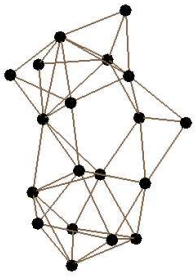

7th

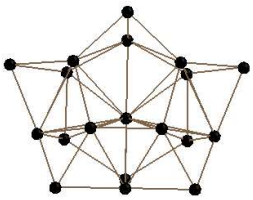

8th

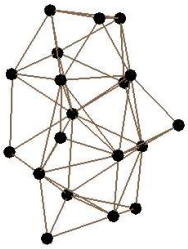

9th

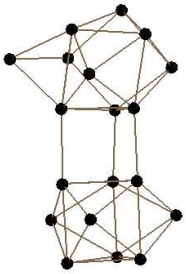

10th

Figure D.13: Geometries of the 10 lowest Si_{19} isomers.

Bibliography

[1] Isotope-abundance variations of selected elements (IUPAC Technical Report), Pure Appl.Chem. **74(10)**, 1987-2017 (2002).

[2] D.K.Yu, R.Q.Zhang, S.T.Lee, Phys. Rev. B **65**, 245417 (2002).

[3] R.B.Hudgins, M.Imai, M.F.Jarrold, and P.Dugourd, J. Chem. Phys. **111**, 7865 (1999).

[4] A.Tekin, B.Hartke, Phys. Chem. Chem. Phys. **6**, 503 (2004).

[5] S.Yoo, X.C.Zeng, Angew. Chem. Int. Ed. **44**, 1491 (2005).

[6] S.Yoo and X.C.Zeng, J. Chem. Phys. **123**, 164303 (2005).

[7] B.Hartke, J. Phys. Chem. **97**, 9973 (1993).

[8] K.-M.Ho, A.A.Shvartsburg, B.Pan, Z.-Y.Lu, C.-Z.Wang, J.G.Wacker, J.L.Fye, M.F.Jarrold, Nature **392**, 582 (1998).

[9] I.Rata, A.A.Shvartsburg, M.Horoi, T.Frauenheim, K.W.M.Siu, K.A.Jackson, Phys. Rev. Lett. **85**, 546 (2000).

[10] Z. Li and H. A. Scheraga, Proc. Natl. Acad. Sci. U.S.A. **84**, 6611 (1987).

[11] J. Doye and D. Wales, Phys. Rev. Lett. **80**, 1357 (1998).

[12] U. Röthlisberger, W. Andreoni and M. Parrinello, Phys. Rev. Let. **72**, 665 (1994).

[13] A.Sieck, Th.Frauenheim, K.Jackson, phys. stat. sol. (b) **240**, 537 (2003).

[14] K.A.Jackson, M.Horoi, I.Chaudhuri, T.Frauenheim, A.A.Shvartsburg, Phys. Rev. Lett. **93**, 013401 (2004).

[15] A.Tekin and B.Hartke, J. Theor. and Comp. Chemistry **4**, 1119 (2005).

[16] S.Goedecker, J. Chem. Phys. **120** 9911 (2004).

[17] T.J.Lenosky, J.D.Kress, I.Kwon, A.F.Voter, B.Edwards, D.F.Richards, S.Yang and J.B.Adams, Phys. Rev. B **55**, 1528 (1997).

[18] A.A.Shvartsburg, R.R.Hudgins, P.Dugourd, and M.F.Jarrold, Chem. Soc. Rev. **30**, 26 (2001).

[19] Ph.Dugourd, R.R.Hudgins, D.E.Clemmer, and M.F.Jarrold, Rev. Sci. Instrum. **68**, 1122 (1997).

[20] M.F.Jarrold and V.A.Constant, Phys. Rev. Lett. **67**, 2994 (1991).

[21] M.F.Jarrold and J.E.Bower, J. Chem. Phys. **96**, 9180 (1992).

[22] A.A.Shvartsburg, B.Liu, M.F.Jarrold, and K.M.Ho, J. Chem. Phys. **112**, 4517 (2000).

[23] M.F.Jarrold and J.E.Bower, J. Phys. Chem. **92**, 5702 (1988).

[24] Q.L.Zhang, Y.Liu, R.F.Curl, F.K.Tittel, and R.E.Smalley, J. Chem. Phys. **88**, 1670 (1988).

[25] M.F.Jarrold and E.C.Honea, J. Phys. Chem. **95**, 9181 (1991).

[26] A.A.Shvartsburg, B.Liu, M.F.Jarrold, B.Liu, Z.Y.Lu,C.Z.Wang, K.M.Ho, Phys. Rev. Lett. **81**21, 4616 (1998).

[27] R. Schäfer, S. Schlecht, J.Woenckhaus, and J.A.Becker, Phys. Rev. Lett. **76**, 471 (1996).

[28] K.Jackson, A.R.Pederson, D.Porezag, Z.Hajnal, and T.Frauenheim, Phys. Rev. B **55**, 2549 (1997).

[29] I.Vasiliev, S.gt, and J.R.Chelikowsky, Phys. Rev. Lett. **78**, 4805 (1997).

[30] V.E.Bazterra, M.C.Caputo, M.B.Ferrara, and P.Fuentealba, J. Chem. Phys. **117**, 11158 (2002).

[31] C.Pouchan, D.Bégué, D.Y.Zhang, J. Chem. Phys. **121**, 4628 (2004).

[32] A.D.Becke, Phys. Rev. A **38**, 3098 (1988).

[33] J.Perdew, K.Burke and Y.Wang, Phys. Rev. B **54**, 16533 (1996).

[34] J.L.Elkind, J.M.Alford, F.D. Weiss, R.T. Laaksonen and R.E. Smalley, J. Chem. Phys. **87** , 2397 (1987).

[35] L.R.Anderson, S.Maruyama, and R.E.Smalley, Chem. Phys. Lett. **176**, 348 (1991).

[36] S.Maruyama, L.R.Anderson, and R.E.Smalley, J. Chem. Phys. **93**, 5349 (1990).

[37] R.L.Zhou, B.C.Pan, Phys. Rev. B **73**, 045417 (2006).

[38] M.F.Jarrold, J.E.Bower, and K.Creegan, J. Chem. Phys. **90**, 3615 (1989).

[39] K.M.Creegan and M.F.Jarrold, J. Am. Chem. Soc. **112**, 3768 (1990).

[40] M.F.Jarrold, U.Ray, K.M.Creegan, J. Chem. Phys. **93**, 224 (1990).

[41] U.Ray and M.F.Jarrold, J. Chem. Phys. **94**, 2631 (1991).

[42] D.J.Trevor, D.M.Cox, K.C.Reichmann, R.O.Brickman, and A.Kaldor, J. Phys. Chem. **91**, 2598 (1987).

[43] K.Fuke, K.Tsukamoto, F.Misaizu, M.Sanekata, J. Chem. Phys. **99**, 7807 (1993).

[44] B.Liu, Z.Lu, B.Pan, C.Wang, K.Ho, A.A.Shvarstburg, and M.F.Jarrold, J. Chem. Phys. **109**, 9401 (1998).

[45] J.Müller, B.Liu, A.A.Shvartsburg, S.Ogut, J.R.Chelikowsky, K.W.M.Siu, K.M.Ho, and G.Gantefor, Phys. Rev. Lett. **85**, 1666 (2000).

[46] O.Cheshnovsky, S.H.Yang, C.L.Pettiette, M.J.Craycraft, Y.Liu, and R.E.Smalley, Chem. Phys. Lett. **138**, 119 (1987).

[47] N.Binggeli and J.R.Chelikowsky, Phys. Rev. Lett. **75**, 493 (1995).

[48] G.Meloni, M.Ferguson, S.Sheehan, D.M.Neumark, Chem. Phys. Lett. **399**, 389 (2004).

[49] R.W.Schmude, Q.Ran, K.A.Gingerich, and J.E.Kingcade, J. Chem. Phys. **102**, 2574 (1995).

[50] Q.Ran, R.W.Schmude, M.Miller, and K.A.Gingerich, Chem. Phys. Lett. **230**, 337 (1994).

[51] T.Bachels and R.Schfer, Chem. Phys. Lett. **324**, 365 (2000).

[52] E.C.Honea, A.Ogura, C.A.Murray, K.Raghavachari, W.O.Sprenger, M.F.Jarrold, and W.L.Brown, Nature **366**, 42 (1993).

[53] S.Li, R.J.Van Zee, W.Weltner Jr. and Krishnan Raghavachari, Chem. Phys. Lett. **275**, 243 (1995).

[54] K.Jackson, M.Pederson, D.Porezag, Z.Hajnal, T.Frauenheim, Phys. Rev. B **55**, 2549 (1997).

[55] S.H.Vosko, L.Wilk, M.Nusair, Can.J.Phys. **58**, 1200 (1980).

[56] A.D.Becke, J. Chem. Phys. **98**, 5648 (1993).

[57] Tao Pang, An Introduction to Computational Phyics, Cambridge University Press (2006).

[58] Cheng L., W.Cai and X.Shao, Chem. Phys. Lett. **389**, 309 (2004).

[59] N.Mousseau, G.T.Barkema, Phys.Rev. E **57**, 2419 (1998).

[60] R.Malek, N.Mousseau, Phys.Rev. E **62**, 7723 (2000).

[61] J.P.K.Doye and D.J.Wales, Z.Phys.D: At., Mol. Clusters **40**,194 (1997).

[62] K.Raghavachari, J. Chem. Phys. **83**, 3520 (1985).

[63] K.Raghavachari and V.Logovinsky, Phys. Rev. Lett. **55**, 2853 (1985).

[64] K.Raghavachari, C.M.Rohlfing, J. Chem. Phys. **89**, 2219 (1988).

[65] C.M.Rohlfing, K.Raghavachari, J. Chem. Phys. **96**, 2114 (1992).

[66] D.M.Deaven, K.M.Ho, Phys. Rev. Lett. **75**, 288 (1995).

[67] Th.Frauenheim, F.Weich, Th.Köhler, S.Uhlmann, D.Porezag, G.Seifert, Phys. Rev. B **52**, 11492 (1995).

[68] A.Sieck, D.Porezag, Th.Frauenheim, M.R.Pederson, K.Jackson, Phys. Rev. A **56**, 4890 (1997).

[69] Jeffrey Grossman and Lubos Mitas, Phys. Rev. Lett. **74**, 1323 (1995).

[70] L.Mitas, J.C.Grossmann, I.Stich and J.Tobik, Phys. Rev. Lett. **84**, 1479 (2000).

[71] J.Jeong, I.Lee, J.Oh, K.Chang, J.Phys.: Condens. Matter **10**, 5851 (1998).

[72] S.Yoo, J.Zhao, J.Wang, X.C.Zeng, J. Am. Chem. Soc. **126**, 13845 (2004).

[73] H.Grubmueller, Phys. Rev. E **52**, 2893 (1995).

[74] A.Voter, J. Chem. Physics **106**, 4665 (1997).

[75] A.Laio and M.Parrinello, Proc.Natl.Acad.Sci.U.S.A.**99**, 12562 (2002).

[76] D. Wales and J. Doye, J. Phys. Chem. A **101** 5111 (1997).

[77] J. Doye, D. Wales, and M. Miller, J. Chem. Phys. **109**, 8143 (1998).

[78] S.Yoo and X.C.Zeng, J. Chem. Phys. **119**, 1442 (2003).

[79] O.F.Sankey, D.J.Niklewski, D.A.Drabold, and J.D.Dow, Phys. Rev. B **41**, 12750 (1990).

[80] R.Fournier, S.B.Sinnott, and A.E.DePristo, J. Chem. Phys.**97**, 4149 (1992).

[81] X.Zhu and X.C.Zeng, J. Chem. Phys. **118**, 3558 (2003).

[82] X.L.Zhu, X.C.Zeng, Y.A.Lei, and B.Pan, J. Chem. Phys. **120**, 8985 (2004).

[83] Nisanth N. Nair, Thomas Bredow and Karl Jug, J. Comput. Chem. **25**, 1255 (2004).

[84] B.-X.Li, J.-H.Liu and S.-C.Zhan, Eur. Phys. J. D **32**, 59 (2005).

[85] K. Raghavachari and C.M. Rohlfing, J. Chem. Phys. **94**, 3670 (1991).

[86] The Cambridge Cluster Database http://brian.ch.cam.ac.uk/CCD.html.

[87] B. Delley: J. Chem. Phys. **92**, 508 (1990).

[88] B. Delley: J. Chem. Phys. **113**, 7756 (2000).

[89] CPMD Version 3.3: developed by J. Hutter, A. Alavi, T. Deutsch, M. Bernasconi, S. Goedecker, D. Marx, M. Tuckerman and M. Parrinello, Max-Planck-Institut für Festkörperforschung and IBM Zürich Research Laboratory (1995-1999).

[90] The code is free software and can be downloaded from http://cp2k.berlios.de/quickstep.html.

[91] J.Perdew, K.Burke and M.Ernzerhof, Phys. Rev. Lett **77**, 3865 (1996).

[92] S.Goedecker, M.Teter, J.Hutter, Phys. Rev. B **54**, 1703 (1996).

[93] T.J.Lenosky, B.Sadigh, E.Alonso, V.Bulatov, T.Diaz de la Rubia, J.Kim, A.F.Voter adn J.D.Kress, Modelling Simul. Mater. Sci. Eng. **8**, 825 (2000).

[94] R.R.Hudgins, M.Imai, M.F.Jarrold and P.Dugourd, J. Chem. Phys. **111**, 7865 (1999).

[95] Z.Li, H.Scheraga, Proc. Natl. Acad. Sci. USA **84**, 6611 (1987).

[96] J. Doye and D. Wales, Phys. Rev. Lett. **80**, 1357 (1998).

[97] S. Goedecker, T. Deutsch and L. Billard, Phys. Rev. Lett. **88**, 235501 (2002).

[98] Bernd Hartke, Angewandte Chemie International Edition **41**, 1468 (2002).

[99] S. Goedecker, W.Hellmann and Thomas Lenosky, Phys. Rev. Lett. **95**, 055501 (2005).

[100] J.R. Trail and R.J. Needs, J. Chem. Phys. 122, 174109 (2005).

[101] http://www.msg.ameslab.gov/GAMESS/.

[102] C. J. Umrigar and C. Filippi. Phys. Rev. Lett. 94, 150201 (2005).

[103] U.Röthlisberger *et al.*, J. Chem. Phys. **96**, 1248 (1992).

[104] J.Jeong *et al.*, J.Phys.: Condens. Matter **10**, 5851 (1998).

[105] M. Jarrold and E. Bower, J. Phys. Chem **92**, 5702 (1988).

[106] Gaussian 03, Revision B.01, M. J. Frisch, G. W. Trucks, H. B. Schlegel, G. E. Scuseria et al. Gaussian, Inc., Pittsburgh PA, 2003.

[107] The formulas for the rotational and vibrational free energy are given in standard textbooks, see for example F.Jensen, Introduction to Computational chemistry (Wiley, New York, 1999).

[108] F.Baletto and R. Ferrando, Rev. Mod. Phys. **77**, 371 (2005).

Acknowledgment

I am indebted to many different people for their support and guidance during the time which I spent working on my PhD thesis. I am particularly grateful to Prof. S.Goedecker for his continuous encouragement and stimulating discussions as well as for his helpful remarks and critical comments. The assignment to the interesting research topic gave me a lot of motivation and I have fully enjoyed the possibility of working within a friendly environment.

I thank Prof. C.Bruder for kindly accepting to co-referee this thesis and Prof. B.Hartke for kindly accepting being an external expert.

I thank the Swiss National Science Foundation for the financial support of my research work.

I would also like to thank M.Jacquot for his technical support and assistance.

I thank X.C.Zeng, K.A.Jackson and A.Tekin for sending us detailed information about their silicon clusters as well as for valuable comments.

I am grateful to my parents for their continuous support.

I should thank the secretaries of the institute of physics Frau Kammermann and Frau Kalt for their friendliness.

I am grateful to my office mate Shantanu Roy for interesting discussions during countless coffee breaks we had.